SARS-CoV-2 infection of the brain: the K18-hACE2 mouse model to illustrate the role and response of the vasculature in neurotropic viral infection

Simon De Neck[1,2], Rebekah Penrice-Randal[1,3], Udo Hetzel[1], Frauke Seehusen[1], Parul Sharma[4], Eleanor G. Bentley[4], Barbara Helminger[1], Adam Kirby[4], Giuseppe Balistreri[5,6], James P. Stewart[4], Anja Kipar[1,4]

[1] Laboratory for Animal Model Pathology, Vetsuisse Faculty, Institute of Veterinary Pathology, University of Zurich, 8057 Zurich, Switzerland

[2] Graduate School for Cellular and Biomedical Sciences, University of Bern, Bern, Switzerland

[3] Department Biochemistry, Cell & Systems Biology, Institute Systems, Molecular & Integrative Biology, 102, Biosciences Building, Crown Street, Liverpool L69 7ZB, United Kingdom

[4] Department of Infection Biology & Microbiomes, Institute of Infection, Veterinary and Ecological Sciences, University of Liverpool, Liverpool L3 3RF, United Kingdom

[5] Department of Virology, Faculty of Medicine, University of Helsinki, 00014 Helsinki, Finland

[6] School of Biomedical Sciences, The University of Queensland, Brisbane, QLD 4072, Australia

Corresponding author: anja.kipar@uzh.ch

Abstract

Severe Acute Respiratory Syndrome Coronavirus 2 (SARS-CoV-2) primarily affects the respiratory tract and lungs; however, the associated disease, coronavirus disease 2019 (COVID-19) can also involve the central nervous system. The pathomechanisms underlying neurological impairments in COVID-19 and post COVID-19 condition remain incompletely understood, hence experimental studies under defined conditions, in a suitable animal model, can help to clarify the effect of SARS-

CoV-2 infection in the brain. The K18-hACE2 mouse represents such a model, as intranasal challenge with SARS-CoV-2 VOC generally results in widespread neuronal infection with limited tissue response in the brain, consistent with a mild non-suppurative (meningo)encephalitis, with microgliosis, astrogliosis and (peri)vascular leukocyte infiltrates but no evidence of infection of vessel structures. The present study used this model to address the hypothesis that the vascular reaction is secondary to the neuronal infection. It confirmed that in intranasally challenged K18-hACE2 mice the virus targeted the neurons without overt neuropathic effect, whilst sparing the blood vessels, and further characterised the resulting inflammatory response in the brain in situ and through bulk RNA sequencing. The former highlighted the recruitment of leukocytes (neutrophils, monocytes/macrophages, and lymphocytes) via postcapillary venules, with their accumulation in the perivascular space and occasional emigration into the neuroparenchyma, without targeting and/or damage to the vessel wall. At the transcriptome level, this was accompanied by positive enrichment of pathways and the upregulation of genes involved in both the inflammatory reaction and the recruitment (including adhesion and migration) and activity of the leukocytes. We also found morphological and molecular evidence of subtle impairment of blood-brain barrier function, i.e. increased permeability. The results obtained from the model indicate that SARS-CoV-2 infection of the neurons induces neuroinflammation, with leukocyte recruitment and activation as well as blood-brain barrier dysfunction. These data can help to understand more fully the reaction of the CNS in COVID-19 patients, and neurotropic virus infections in general.

Keywords: SARS-CoV-2, K18-hACE2 mouse, brain, neuroinflammation, blood vessels, bulk RNA sequencing, transmission electron microscopy, transcriptome, brain infection

Introduction

51 Severe Acute Respiratory Syndrome Coronavirus 2 (SARS-CoV-2) primarily affects the respiratory
52 tract and lungs; however, other organ systems including the central nervous system (CNS) can also
53 be involved in the associated disease, coronavirus disease 2019 (COVID-19) [1, 2]. Indeed,
54 neurological and neuropsychiatric symptoms have been observed and still are a concern not only in
55 patients with acute COVID-19 but also with Long COVID (also known as post COVID-19 condition)
56 [2–6]. The pathomechanisms underlying the neurological impairments remain incompletely
57 understood. Several have been proposed, one of them involving direct viral CNS infection, although
58 this is overall considered a very rare event [2, 7]. In the case of Long COVID, some publications
59 suggest that the condition has a psychosomatic component [8–10].

60 Several original publications and reviews report on the pathological changes in the brain in fatal
61 COVID-19 cases; they were summarised and interpreted as "a pattern of cerebrovascular pathology
62 and microglial-predominant inflammation" [11, 12]. Histologically, (sub)acute infarcts and hypoxic-
63 ischaemic injury, microthrombi, acute (micro)haemorrhages, microglial activation and occasional
64 microglial nodules as well as mild lymphocyte-dominated perivascular, parenchymal and meningeal
65 inflammatory infiltrates have been described [11–19]. Interestingly though, in the majority of cases
66 the virus was either not detectable in the brain, or present in minimal amounts, as determined by
67 various methodological approaches, RT-PCR, droplet digital PCR, *in situ* hybridisation and/or
68 immunohistochemistry [11, 12]. Indeed, the debate on the frequency and extent of SARS-CoV-2
69 infection of the brain in COVID-19 patients has still not come to a conclusion. However, an in-depth
70 study on the distribution of SARS-CoV-2 in autopsied fatal COVID-19 cases reported the presence of
71 viral protein and RNA in the brain of several patients that died within the first few weeks of clinical
72 disease. The study also demonstrated persistence of viral RNA in the brain of a patient examined 230
73 days after the onset of symptoms [20]. Interestingly, the presence of virus in the brain was not
74 associated with relevant inflammatory changes or evidence of a viral cytopathic effect [20], whereas
75 in a slightly earlier study by a different group perivascular T cell (CD4+ and CD8+ cells) and
76 macrophage infiltrates were reported from fatal COVID-19 cases [14]. Neurons have been shown to

77 become infected, and there are reports that claim infection also of non-neuronal cells, such as
78 ependymal cells, vascular endothelial cells or pericytes, and even glial cells, often aligned with the
79 expression pattern of the viral receptor angiotensin-converting enzyme 2 (ACE2) [14, 20–23].

80 Considering the relevance and variability of clinical CNS signs in patients with acute COVID-19
81 and Long COVID, the evidence that neuronal viral infection without overt neuronal damage and/or
82 substantial inflammatory response can occur in COVID-19, and the partly controversial data on viral
83 target cells in the brain, experimental studies under defined conditions, in a suitable animal model,
84 can help to clarify some open questions regarding SARS-CoV-2 infection of the CNS, and neurotropic
85 viral infections in general. Several groups including ours have previously shown that intranasal
86 challenge of K18-hACE2 mice (expressing human (h)ACE2 under the K18 promotor [24]) with SARS-
87 CoV-2 variants, i.e. original and variant of concern (VOC) isolates, results in rather consistent spread
88 to the brain [25–40]. Evidence of neurological signs and morphological features consistent with
89 neuronal cell death were observed, but only at high viral doses (10^6 PFU) [25]. Viral antigen and RNA
90 was detected in neurons in infected brains [25, 26, 30, 33–38, 40], however, each one study also
91 reported infection of astrocytes and microglia, though this was apparently not prominent [30],
92 infection of endothelial cells [37] and some immunostained macrophages [35]. Despite widespread
93 neuronal infection, the brain parenchyma exhibited only a limited reaction, consisting mainly of a
94 mild (meningo)encephalitis, microgliosis and astrogliosis [25–27, 30, 34–36, 38], similar to what has
95 been reported in some fatal COVID-19 cases [13, 20].

96 It cannot be ruled out that SARS-CoV-2 is neurotropic in humans [7], also, several modes of
97 virus entry into the CNS have been discussed: 1) transsynaptic neuronal /retrograde axonal transport
98 via nerves; 2) haematogenous, across the blood-brain barrier (BBB), using ACE2 as receptor, or via
99 infected leukocytes; 3) from meninges and circumventricular organs, via the cerebrospinal fluid [41–
100 43]. In the widely used K18-hACE2 model, there is strong evidence that SARS-CoV-2 reaches the
101 brain, at least in part, via the olfactory system and spreads among neurons [25, 26, 44, 45]. This is
102 supported by the fact that invasion of the brain in mice is only seen after intranasal challenge and

103 not after exposure to aerosolized SARS-CoV-2 (Fumagalli et al. 2022). As a model of non-
104 haematogenous brain entry, the K18-hACE2 mouse allows to study the mechanism of neuronal
105 infection and spread as well as the direct parenchymal response to infection of the brain.

106 Based on previous work done by our group, we hypothesised that the vessel-centred reaction in
107 the brain of SARS-CoV-2 infected K18-hACE2 mice is a response to the neuronal infection, rather
108 than a targeting of the blood vessels by the virus and/or leukocytes. To test this hypothesis, we used
109 original SARS-CoV-2 Pango B lineage and Delta variant infected K18-hACE2 mice to explore the role
110 of cerebral blood vessels in brain infection, with special emphasis on leukocyte recruitment, integrity
111 of the vascular wall, and maintenance of BBB function.

112

113

114 Material and Methods

115 **Viruses**

116 For the present study, a Pango B lineage UK isolate of SARS-CoV-2 (hCoV-
117 2/human/Liverpool/REMRQ0001/2020; subsequently referred to as "Pango B") and a Delta (VOC)
118 isolate (B.1.617.2 hCoV-19/England/SHEF-10E8F3B/2021; GISAID accession number
119 EPI_ISL_1731019) were used for experimental infections [26, 46]. Both have previously been shown
120 to spread to the brain with high frequency and induce a mild non-suppurative encephalitis and
121 meningitis in a proportion of affected mice [26, 47].

122

123 **Animals and virus infection**

124 Animal work was approved by the local University of Liverpool Animal Welfare and Ethical Review
125 Body and performed under UK Home Office Project Licence PP4715265. It was undertaken in
126 accordance with locally approved risk assessments and standard operating procedures. The study
127 was undertaken on mice carrying the human ACE2 gene under the control of the keratin 18
128 promoter (K18-hACE2; formally B6.Cg-Tg(K18-ACE2)2Prlmn/J) purchased from Charles River

129 Laboratories (Wilmington, Massachusetts, USA). Mice were maintained in biosafety level 3 facilities
130 under SPF barrier conditions in individually ventilated cages.

131 The study was undertaken on cohorts of K18-hACE2 mice that were part of experimental
132 infections undertaken for other projects (cohorts 1.1 to 1.4), or specifically recruited for the present
133 study (cohorts 2.1 to 2.3) (Table 1).

134 For infections, mice were anaesthetized lightly with isoflurane and inoculated intranasally
135 with 50 µl sterile PBS containing virus isolate at different doses (Table 1). Mock infected mice,
136 injected intranasally with 50 µl sterile PBS, served as controls. The mice were monitored daily for
137 clinical signs, weighed and were sacrificed by an overdose of pentobarbitone after reaching the
138 clinical endpoint (maximum of 20% loss of body weight), or at the end of the experiment, at 4, 5, 6, 7
139 or 8 days post infection (dpi) (Table 1). Mice were dissected immediately after death and the brain
140 and lungs collected and sampled for downstream processing.

141

142 **Table 1**. Study cohorts, and investigations undertaken.

Cohorts	Virus	PFU	DPI: animal no (sex)	Investigations
1.1	Pango B	10^3	**6**: 1.1.1 - 1.1.6 (F)	H, IHa
1.2	Pango B	10^4	**4**: 1.2.1, 1.2.2 (M); 1.2.3 - 1.2.5 (F) **6**: 1.2.6 - 1.2.9 (M); 1.2.10 - 1.2.13 (F)	H, IHa
1.3	Delta	10^3	**5**: 1.3.1 (M); 1.3.2 (F) **6**: 1.3.3, 1.3.4 (M); 1.3.5 - 1.3.11 (F) **7**: 1.3.12, 1.3.13 (M); 1.3.14 - 1.3.17 (F)	H, IHa, IHb; RT-qPCR
1.4	Mock	-	**7**: 1.4.1, 1.4.2 (M); 1.4.3, 1.4.4 (F)	H, IHa; RT-qPCR
2.1	Delta	10^2	**6**: 2.1.1 - 2.1.3 (F) **7**: 2.1.4 - 2.1.8 (F)	H, IHa, IHb, IHc; RT-qPCR; RNAseq, TEM, immune-EM
2.2	Delta	10^3	**7**: 2.2.1 (F) **8**: 2.2.2 - 2.2.5 (F)	H, IHa, IHb; TEM
2.3	Mock	-	**7**: 2.3.1 - 2.3.6 (F)	H, IHa, IHc; RNAseq, TEM, immune-EM

143 Female and male K18-hACE2 mice, aged 6-8 weeks, were intranasally infected with different doses
144 of a SARS-CoV-2 Pango B or Delta VOC isolate, or mock infected, and euthanised at different time
145 points post infection.

146 **Abbreviations**: Animal no: animal number for identification of individual mice; B: brain; DPI - days
147 post postinfection (day of euthanasia); Delta: SARS-CoV-2 Delta isolate; F: female; H: histological
148 examination of the brain (HE-stained section); IHa: immunohistochemistry for SARS-CoV-2
149 nucleocapsid protein (NP), as previously described [26], performed on sections of the brain; IHb:
150 immunohistochemistry for leukocyte markers (Iba1, CD3, CD4, CD8, Ly6G) and apoptotic cells
151 (cleaved caspase 3), as previously described [26, 48, 49], performed on sections of the brain; IHc:
152 immunohistochemistry for markers of blood vessels/blood-brain-barrier (PECAM-1/CD31, Claudin 5,
153 PDGFR-β, α-SMA, AQP4) (see Supplemental Table S1), performed on sections of the brain; immune-
154 EM: immune electron microscopy for SARS-CoV-2 nucleocapsid protein performed on the brain; L –
155 lung; Pango B – Pango B lineage UK isolate of SARS-CoV-2; PFU - plaque-forming units; M: male;
156 Mock: mock infected; RNAseq: RNA sequencing performed on the brain; RT-qPCR: reverse
157 transcriptase-quantitative PCR for SARS-CoV-2 N1 [47] performed on lung and brain tissue; TEM:
158 transmission electron microscopy performed on the brain.
159
160 **Tissue processing**
161 From all mice, the left lung was fixed in 10% neutral buffered formalin (NBF) whereas the right lung
162 was frozen at -80 °C for RT-qPCR. In cohorts 1.3, 1.4 and 2.1, a sample from the frontal cortex was
163 collected and frozen at -80 °C for RT-qPCR. The remaining brain of animals from cohort 1.3 as well as
164 the whole brains in cohorts 1.1, 1.2 and 1.4 were fixed in 10% NBF. For all mice of cohorts 2.1 to 2.3,
165 a slice of brain (approximately 1 mm thickness) was prepared by coronal sections at the level of the
166 hippocampus and the thalamus (one section rostral, the second caudal to the pituitary ring) from
167 which a sample (2-3 mm^3) from the thalamic region was cut out and fixed in 5% glutaraldehyde (GA)
168 (buffered in 0.2 M cacodylic acid buffer, pH 7.3) for transmission electron microscopy (TEM); for
169 mice of cohorts 2.1 and 2.3, another sample was collected and frozen at -80 °C for RNA sequencing.
170 The remaining brain tissue was fixed in 10% NBF. Information on the animals and the tissue
171 processing and examination is provided in Table 1.

172

173 **Quantitative RT-PCR for viral load**

174 SARS-CoV-2 viral loads were determined in the right lung and frontal cortex tissue samples of
175 cohorts 1.3, 1.4 and 2.1 that had been stored at -80 °C, using the GoTaq® Probe 1-Step RT-qPCR
176 System (Promega). For quantification of SARS-COV-2 the nCOV_N1 primer/probe mix from the SARS-
177 CoV-2 (2019-nCoV) CDC qPCR Probe Assay (IDT) and murine 18S primers were utilised as described
178 previously [47]. All analyses were done in duplicate.

179

180 **Histological and immunohistological examinations**

181 All NBF fixed tissue samples were transferred to 70% ethanol after 24-48 h fixation, until further
182 processing. The brain was trimmed by one sagittal or several coronal sections (cohorts 1.1-1.4), or
183 coronal sections (cohorts 2.1-2.3), to allow evaluation of representative brain regions including the
184 olfactory bulb. These as well as the left lungs were then routinely paraffin wax embedded.
185 Consecutive sections (3-4 µm) were prepared and stained with haematoxylin and eosin (HE) or
186 subjected to immunohistochemistry (IHC). All lungs (for confirmation of infection) and brains were
187 stained for SARS-CoV-2 nucleocapsid protein (NP), as previously described [26]. In addition, brains
188 from cohorts 2.1-2.3 were selectively stained to identify infiltrating leukocytes, i.e. Iba1
189 (monocytes/macrophages, microglia), CD3 (T cells), CD4 (helper T cells), CD8 (cytotoxic T cells), and
190 Ly6G (neutrophilic leukocytes), and apoptotic cells (cleaved caspase 3), as previously described [26,
191 48, 49]. These stains served to confirm that this set of experimental infections resulted in the same
192 changes as those previously described by our group and in human patients [13, 26]. The brains of
193 cohorts 2.1 (10^2 SARS-CoV-2 Delta) and 2.3 (mock infected) were also stained for the expression of
194 blood vessel/BBB markers, i.e. platelet endothelial cell adhesion molecule 1 (PECAM-1/CD31;
195 endothelial cells), claudin 5 (tight junction protein), platelet-derived growth factor receptor beta
196 (PDGFR-β) and alpha smooth muscle actin (αSMA) (leiomyocytes, pericytes), and aquaporin 4
197 (astrocytic endfeet; AEF) [50–55]. Briefly, after deparaffination, antigen retrieval was performed

198 with citrate buffer (pH 6.0), Tris-EDTA buffer (pH 9.0), or Cell Conditioning Solution (CC1) (pH 9.0).
199 Then, sections were incubated with the primary antibodies diluted in Dilution buffer (Agilent Dako,
200 Santa Clara, California, USA) at different temperatures and lengths of time. Subsequently,
201 endogenous peroxidase was blocked using the Peroxidase Blocking Solution (Agilent Dako) for 10
202 min at room temperature (RT), followed by incubation with the appropriate secondary antibody and
203 detection system, either in the Autostainer Link 48 (Agilent Dako) or the Discovery XT
204 (Roche/Ventana, Basel, Switzerland) and counterstaining with haematoxylin. Information on the
205 primary antibodies, antigen retrieval method, and the detection systems is provided in
206 Supplementary Table S1. The following positive controls were used: a mouse lung previously tested
207 positive for SARS-CoV-2 NP, and a mouse spleen for the leukocyte markers and cleaved caspase 3;
208 for all other markers, the brain parenchyma served as internal positive controls. Negative control
209 sections were incubated without the primary antibody in the diluent; lungs from uninfected control
210 mice served as negative controls for SARS-CoV-2 NP.

211 The HE stained brain sections, together with the sections immunostained for SARS-CoV-2 NP
212 were examined blindly and, besides a general histological examination, specifically assessed for the
213 presence of (peri)vascular leukocyte infiltrates and for viral antigen expression. In the CNS, the
214 "perivascular space" is a defined structural entity [56]. Therefore, in the present study, we speak
215 about a "perivascular infiltrate" when leukocytes are located between the external layer of a vessel
216 wall and the AEF. We apply the term "vascular infiltrate" when leukocytes are located within the
217 vessel wall (which we and others have so far also referred to as "vasculitis" [26, 35, 38]). However, as
218 it is often difficult to unequivocally distinguish between leukocytes located within the vascular wall
219 and in the perivascular space in light microscopical specimens (in contrast to thin sections examined
220 by electron microscopy), we speak about (peri)vascular infiltrates in particular when referring to HE
221 stained sections.

222 In order to allow a basic comparison between the extent of viral antigen expression and viral
223 loads determined by RT-qPCR, the IHC-determined NP expression and distribution pattern was semi-

224 quantitatively graded as a) negative (no immunostaining); b) scattered (variable number of
225 individual positive neurons); c) clusters (variable numbers of groups of positive neurons); d)
226 widespread (large/coalescing patches of positive neurons). The expression pattern is illustrated in
227 Supplemental Figure S1.
228
229 **Transmission electron microscopy (TEM) including immune-EM**
230 GA-fixed brain specimens from cohorts 2.1-2.3 were routinely embedded in epoxy resin. Semithin
231 sections (0.95 µm) were prepared from the epoxy blocks and stained with toluidine blue to select
232 the areas of interest (i.e. areas including blood vessels with or without (peri)vascular infiltrates) for
233 the ultrathin sections (95 nm). The latter were prepared and contrasted with lead citrate and uranyl
234 acetate. The ultrathin sections were viewed with a Philips CM10 microscope and digital images taken
235 with a Gatan Orius SC1000 digital camera (Gatan Microscopical Suite, Digital Micrograph, California,
236 USA).
237 The ultrathin sections were subjected to extensive screening of the blood vessels to
238 determine any potential pathological changes, such as the presence of (peri)vascular leukocytes,
239 changes at the level of the AEF, and morphological alterations of the blood vessel wall. The number
240 of blood vessels chosen for further assessment and imaging ranged from 12 to 59 per brain
241 (depending on the number of vessels in the sections). Images were taken from vessels primarily
242 based on the presence of the following features: (peri)vascular leukocytes, evidence of AEF at
243 section level, viral particles in cells adjacent to the vessels and/or changes suggestive of cell
244 degeneration/death. In addition, blood vessels without apparent changes were included. For the
245 subsequent in-depth assessment of the vessels, a two-step process was applied. First, the normal
246 appearance of the blood vessels/BBB in the K18-hACE2 mice was determined, using literature as a
247 reference [57–65]. Here, the vessels in the brains of the mock infected control mice (2.3) served for
248 the comparative assessment of vessels in the Delta infected (cohorts 2.1 and 2.2) brains. In a second
249 step, a qualitative review of all examined vessels was undertaken, focusing on the following

250 morphological features: alteration of the vascular wall (cell degeneration/death, alteration of the
251 endothelial tight junctions), changes at the level of the AEF (swelling, glycogen accumulation),
252 presence of leukocytes (in the vascular wall, the perivascular space, or the adjacent
253 neuroparenchyma), presence of viral particles (at any level of the vessel wall, in cells adjacent to the
254 vessel).

255 A GA-fixed, epoxy resin embedded pellet of human embryonic kidney (HEK-293T) cells
256 transduced to stably express the human ACE2 receptor, and infected with SARS-CoV-2 Omicron
257 Xbb.1.5 at a dose of 5 MOI (multiplicity of infection, PFU/cell) and collected at 72 h post infection
258 [66], served as positive control, i.e. as reference for viral structures at different stages of the viral
259 cycle in cells in the brains (Supplemental Figure S2).

260 For immune-EM, ultrathin sections were prepared from the brains of cohorts 2.1 and 2.3 and
261 incubated with citrate buffer (pH 6.0; Agilent Dako) at 60 °C for 7 h, followed by a 30 min incubation
262 at RT in Antibody Diluent (Agilent Dako) and an overnight incubation at 4 °C with the rabbit anti-
263 SARS-CoV-2 NP antibody used for IHC at a dilution of 1:1,000. Sections were subsequently washed
264 with Wash Buffer 10x (Agilent Dako) and incubated with the secondary antibody (12 nm Colloidal
265 Gold AffiniPure™ Goat Anti-Rabbit IgG (H+L), Jackson ImmunoResearch Laboratories Inc., Ely, UK),
266 diluted 1:30 in Antibody Diluent for 2 h at RT. The sections were contrasted and examined as
267 described above.

268 The infected hACE2 transfected HEK-293T cell pellet (see above) served to establish the immune-EM
269 protocol and to define the optimal primary antibody concentration. Sections of the pellet and brains
270 incubated without the primary antibody as well as the brains of cohort 2.3 served as negative
271 controls.

272

273 **RNA sequencing and bioinformatic analysis**

274 RNA was extracted as previously described [47]. Illumina RNA sequencing was undertaken by
275 Novogene (Novogene (UK) Company Limited, Cambridge, UK) on the samples collected from the

276 coronal brain slice for animals in cohorts 2.1 and 2.3, using polyA enrichment and the NovaSeq X
277 Plus (Illumina®, San Diego, California, USA). Sequencing reads were trimmed with fastp (v0.24.0,
278 [67]). Trimmed paired end sequencing reads were inputted into salmon (v1.10.3, [68]) using the -l A
279 –validateMappings –SeqBias –gcBias parameters with the "Mus_musculus.GRCm39.cdna.all.fa"
280 reference sequence. Quant files generated with salmon were imported into RStudio (RStudio:
281 Integrated Development Environment for R, version 4.4.4, Posit Software, PBC, Boston,
282 Massachusetts, USA) (4.4.4) using tximport to infer gene expression (v1.32.0, [69]). After import of
283 the matrix of genes counts in RStudio (RStudio: Integrated Development Environment for R, version
284 2024.09.1 Build 394), R [70] was used to perform all the transcriptomic analyses. The filtering of
285 genes with low or no counts and the normalisation of the libraries size was done with the edgeR
286 package (v4.2.1, [71]), using the filterByExpr() and calcNormFactors() functions. Visualisation and
287 clustering of the samples was investigated with a principal component analysis (PCA), on log_2-
288 transformed counts per million (log_2 CPM), using the PCAtools package (v2.16.0, [72]). Testing for
289 differential gene expression was carried out using the exactTest() function from the edgeR package
290 (v4.2.1, [71]). Genes were considered as differentially expressed when showing at least a 2-fold
291 difference ((log_2FC)) from the mock infected group, with a false discovery rate (FDR) below 0.05. The
292 results of the differential gene expression was visualised with a volcano plot (EnhancedVolcano
293 package: v1.22.0 [73]). The differentially expressed genes were filtered by log_2FC (>2 or <-2) and FDR
294 (<0.05), and the corresponding log_2 CPM of the 20 most significantly upregulated and
295 downregulated genes were visualised with heatmaps (pheatmap package: v1.0.12 [74]). Pathway
296 enrichment analysis was performed on a gene list sorted by decreasing values of log_2FC (Gene Set
297 Enrichment Analysis (GSEA)), for both Gene Ontology (GO) and Kyoto Encyclopedia of Genes and
298 Genomes (KEGG), using the gseGO() and gseKEGG() functions from the clusterProfiler package
299 (v4.12.6; [75]), with the adjusted p-value cut-off set at 0.05. Visual investigation of selected KEGG
300 pathways was performed using the pathview package (v1.44.0; [76]). The code used to analyse the

301 data is available on request. A list of the packages used is available in the supplemental material
302 (Supplemental Table S2). Sequencing reads are available under BioProject ID: PRJNA1220666.
303 In the subsequent analysis, we focused on pathways and specific genes that were of interest
304 in the context of inflammation and the recruitment of leukocytes into the brain, and on those that
305 would acknowledge differences in vascular permeability and BBB alterations. For the pathways, the
306 results of the GO GSEA analysis were subjected to a manual review and potential pathways of
307 interest were marked. From this selection, pathways of the biological process (BP) ontology were
308 extracted in RStudio and further classified into three categories, using manually curated lists of
309 keywords, namely: 1) inflammatory mediators; 2) leukocytes; 3) blood vessels and BBB. The resulting
310 selection for each category was manually reviewed to remove duplicated pathways (the pathway
311 considered as the most representative of a given biological process was kept) and the top 20
312 pathways (sorted by normalised enrichment score (NES)) for each category (and sub-category when
313 it applies) were plotted. A similar approach was taken for the results from the KEGG GSEA analysis,
314 except that due to the lower number of pathways of interest, these were not further divided in
315 categories, and all the manually marked pathways were shown.
316 As for the genes of interest, these were selected based from the literature (inferring
317 important genes from the morphological changes observed on light microscopy and TEM), and
318 derived from the GSEA GO and KEGG (GSEA and pathview()) analysis. These genes were organised in
319 three categories, namely: 1) inflammatory mediators [77–80]; 2) leukocyte recruitment factors [56,
320 81]; 3) BBB key components/factors [51, 53, 55, 63, 82–88]. For each category, the genes of interest
321 were extracted from the results of the differential gene expression analysis and in the case of the
322 two first categories, only the genes with a $\log_2$FC >2 and a FDR <0.05 were kept and sorted according
323 to descending $\log_2$FC values; the top 20 genes were subsequently plotted.
324
325
326 **Results**

327 **SARS-CoV-2 infection of lung and brain are not directly correlated**

328 Previous studies, including from our group, have shown and characterised lung and brain infection in
329 K18-hACE2 mice intranasally infected with SARS-CoV-2. Viral RNA was detected in the lung and the
330 brain as soon as 1 and 2 dpi respectively. In the lung, the peak of RNA levels seems to be reached at
331 3 dpi, with lower levels at 5 and 6 dpi; in the brain, the RNA levels increase and are reported to be
332 high from 4 to 7 dpi [25–28, 30–40, 89]. Viral antigen expression seems to follow soon after RNA [36,
333 40].

334 For the present study, we wanted to determine whether the virus spreads to the brain also
335 with lower inoculation doses than those previously applied. We performed the RT-qPCR for SARS-
336 CoV-2 N1 on lung and brain samples of the mice examined at day 5, 6 or 7 dpi with SARS-CoV-2 Delta
337 at 10^3 PFU (cohorts 1.3) (previously applied moderate dose [26]) or 10^2 PFU (low dose; cohort 2.1),
338 respectively. Regardless of the inoculation dose, we generally detected the virus at high copy
339 numbers in the brain (Supplemental Figure S3). This confirmed that intranasal challenge had,
340 consistently, not only led to pulmonary infection but also to spread to the brain (Supplemental Table
341 S3). With the higher infectious dose (cohort 1.3), when animals had reached the clinical endpoint, at
342 5 or 6 dpi, the N1 copy numbers were higher in the lung compared to the brain (Supplemental Figure
343 S3). After the lower dose infection, animals had to be culled at 6 dpi or reached the scheduled end of
344 study, at 7 dpi. Interestingly, in this cohort, the average N1 copy numbers in the lungs were lower at
345 both time points than after the higher dose infection while the brain copy numbers were higher
346 (Supplemental Figure S3). The latter were also higher than those in the lung in this cohort
347 (Supplemental Table S3). As expected, N1 RNA was not detected in the control mice (cohort 1.4). In
348 both mouse cohorts (1.3 and 2.1), brain infection was associated with consistent viral NP expression;
349 indeed, all but one brain showed widespread neuronal virus infection (Supplemental Table S3).

350 The present results confirm that brain infection also occurs at a low inoculation dose with
351 SARS-CoV-2 Delta and indicate that the peaks of viral infection in lungs and brain are not aligned.
352 This could also suggest that the inoculation dose is more relevant for the extent of lung infection

353 than brain infection, and that infection of the brain does not require the lungs to be infected. A
354 previous study has already demonstrated that the inoculation method (intranasal or aerosol)
355 influences the ability of SARS-CoV-2 to reach the brain [30].
356
357 **(Peri)vascular infiltrates occur with widespread neuronal SARS-CoV-2 infection of the brain**
358 Several previous studies have shown that in K18-hACE2 mice SARS-CoV-2 VOC infection of the brain
359 is often accompanied by a mild (meningo)encephalitis, partly with evidence of vasculitis [25–27, 30,
360 34–36, 38]. For the present study we wanted to delve deeper into the inflammatory response
361 associated with infection of the brain in K18-hACE2 mice and blindly (re-)examined brains of
362 intranasally challenged mice between 4-8 dpi for the presence and extent of inflammatory
363 infiltrates; a large proportion of these were retrospectively examined as the animals had been part
364 of other studies, hence viral RNA loads had not been determined.
365 Overall, viral antigen expression was detected in the brain of 85.7% (42/49) of infected mice,
366 across all time points. At 4 dpi (cohort 1.2; infection with 10^4 SARS-CoV-2 Pango B), viral antigen was
367 detected in 4/5 brains, in clusters of infected neurons, with evidence of (peri)vascular infiltrates in
368 one brain. The two mice that had to be culled at 5 dpi with 10^3 SARS-CoV-2 Delta (cohort 1.3)
369 showed widespread neuronal infection, in one of these accompanied by a perivascular inflammatory
370 infiltrate. Almost all mice (23/26) culled at 6 dpi (cohorts 1.1, 1.2, 1.3, and 2.1; infection with 10^3 or
371 10^2 SARS-CoV-2 Delta), whether scheduled or euthanised due to clinical endpoint, harboured viral
372 antigen. In the majority (17/26) widespread neuronal infection was seen; this was generally
373 associated with the presence of (peri)vascular infiltrates (16/17). In mice with the "clusters" pattern
374 (4/26), (peri)vascular infiltrates were seen in half of the cases (2/4), while these were lacking in the
375 mice with the "scattered" pattern (2 mice) or no viral antigen expression (3 mice). The findings were
376 similar in mice culled at 7 dpi (cohorts 1.3, 2.1, and 2.2) and 8 dpi (cohort 2.2), with most of them
377 harbouring viral antigen (in the "widespread" pattern) (13/16); (peri)vascular infiltrates were seen in
378 almost all of these positive cases (12/13), while they were absent in one mouse with the

379 “widespread” pattern and in the three mice not harbouring SARS-CoV-2 antigen. Individual animal
380 data are provided in Supplemental Table S4.
381 As illustrated in Supplemental Figure S1C, (peri)vascular infiltrates were observed in areas of
382 extensive SARS-CoV-2 antigen expression in neurons.
383
384 **SARS-CoV-2 Delta infection of the brain does not target or lead to structural changes in the brain**
385 **vasculature**
386 We subsequently tried to further investigate the leukocyte infiltrates and any potential pathological
387 changes in the endothelium and vascular walls in infected brains. As a first step, we applied IHC to
388 selected brains of cohorts 2.1 and 2.2 and confirmed that the (peri)vascular infiltrates were
389 composed of monocytes/macrophages, T cells and a few neutrophilic leukocytes; the T cell
390 population harboured both CD4 and CD8 positive cells and was found to migrate further, from
391 vessels into the parenchyma (Supplemental Figure S4), all as previously described [13, 26].
392 In order to assess the affected brain vessels for structural damage, we subjected the brains of
393 cohorts 2.1 (SARS-CoV-2 Delta-infected; 6/7 dpi) and 2.3 (mock infected control mice) to
394 immunohistochemical staining for key components of endothelium, vascular wall, and BBB, namely
395 PECAM-1 (endothelial cells), claudin 5 (tight junction protein), PDGFR-β and α-SMA (leiomyocytes,
396 pericytes), and aquaporin 4 (AEF). This did not reveal any differences in expression patterns and
397 extents of any of these markers in vessels with and without inflammatory infiltrates in the infected
398 brains (Figure 1), suggesting the absence of structural alterations of the vessels. However, staining
399 for aquaporin 4 showed that, when present, the (peri)vascular infiltrates were contained within the
400 perivascular space, as these were outlined by a rim of AEF (Figure 1E), cell extensions that represent
401 the outer limit of the perivascular space in the CNS [65]. Staining for PECAM-1, α-SMA, and PDGFR-β
402 suggested the presence of leukocytes within the wall of some affected vessels (Figure 1A, C, D).
403 Transmission electron microscopy (TEM), performed on the same animal cohorts, allowed
404 further characterisation of the vascular response. Vessels affected by (peri)vascular infiltrates were

405 mainly identified as post-capillary venules [56]. Leukocytes, i.e. monocytes/macrophages,
406 neutrophilic leukocytes and lymphocytes, were observed in the vascular lumen and infiltrating the
407 wall, with individual cells beneath the endothelial cell layer (Figure 2). These leukocytes were
408 covered by a continuous endothelial layer, with visible, intact intercellular junctions between
409 adjacent endothelial cells. Rarely, a leukocyte was seen passing through the endothelial layer and
410 the underlying basement membrane (Figure 2C). Leukocytes were also located in the perivascular
411 space, surrounded by a basement membrane and the AEF (Figure 2A-C), or within the adjacent
412 neuroparenchyma (Figure 2D). Occasionally, individual leukocytes in the perivascular space or in the
413 neuroparenchyma adjacent to affected blood vessels were found to be apoptotic (Supplemental
414 Figure S5A-C), confirming what was seen on light microscopy (cleaved caspase 3 IHC) and in our
415 previous study [26].

416 Regardless of the presence or absence of (peri)vascular leukocyte infiltrates, there was no
417 evidence of morphological alterations of the vascular wall in infected brains (Figures 2-4;
418 Supplemental Figure S5B, C).

419 Previous murine studies have provided strong evidence that SARS-CoV-2 infection of the brain
420 is limited to neurons [25, 26, 30, 33, 35–38, 40], however, others claimed that astrocytes, microglia,
421 endothelial cells, and macrophages can also be infected [30, 35, 37]. To address this discrepancy, the
422 present study combined TEM with both IHC and immune-EM for viral NP. Indeed, strong staining for
423 SARS-CoV-2 NP and ultrastructural elements suggestive of virions were observed in neurons
424 immediately adjacent to blood vessels (Figure 3) while neither viral particles nor NP expression were
425 detected in any structures/cells of the blood vessel wall and in surrounding non-neuronal cells,
426 including any emigrating/infiltrating leukocytes (Figures 2 and 3).

427 As part of the detailed ultrastructural examination, specific emphasis was laid on AEF, as an
428 essential component of the BBB [63], with a focus on small calibre vessels (compatible with
429 capillaries and post-capillary venules), as leukocyte recruitment has been reported to take place at
430 the level of post-capillary venules [56]. The examination revealed subtle differences between

431 infected and control brains. The majority of vessels in all examined brains were surrounded by more
432 or less distinct AEF (Figure 4), reflecting the variable thickness of the sheet [90]; when prominent,
433 the AEF were found to contain small amounts of finely granular, electron-dense material (Figure 4)
434 compatible with glycogen [59]. In some infected mice, a few vessels, both with and without
435 (peri)vascular infiltrate, exhibited more prominent AEF containing an increased amount of the
436 granular, electron-dense material (Figure 4).
437
438 **The transcriptomic profile of SARS-CoV-2 Delta infected brains reflects the *in situ* findings**
439 To complement the *in situ* investigation, and to gain better understanding of the molecular changes
440 at play in the infected brains, we performed a bulk RNA sequencing analysis on brains that had been
441 examined in depth at light microscopical and ultrastructural level (cohort 2.1: Delta 10^2 PFU; cohort
442 2.3: mock infected; Supplemental Table S2), on a brainstem sample collected adjacent to the TEM
443 sample. Investigating the transcriptome, we aimed to 1) determine the inflammatory environment
444 associated with brain infection; 2) further characterise the leukocyte recruitment process; 3)
445 determine the state of activation in recruited leukocytes; and 4) detect any transcriptional changes
446 that reflect or are associated with increased BBB permeability.
447 The PCA biplot showed that our samples clustered in two groups according to principal
448 component 1 (PC1) (Figure 5A), corresponding to the Delta infected brains (cohort 2.1) and the
449 brains of mock infected control mice (cohort 2.3) respectively, indicating that brain infection induces
450 a distinct transcriptional profile. Amongst the genes contributing most to the variations were many
451 that highlight inflammatory processes. *Cxcl9*, *Cxcl10*, *Il1rn*, for example, represent chemokines and a
452 cytokine [77, 78]. *Lcn2* encodes for the acute-phase protein like lipocalin 2, a protein that can be
453 produced by several cell types in the brain (microglia, astrocytes, neurons, endothelial cells) and can
454 induce chemokine production; it has been shown to play a role in neuroinflammation,
455 neurodegeneration, and innate immunity [91, 92]. *Slfn4* (Schlafen 4) expression, however, has been
456 shown to be upregulated during macrophage activation [93]. Testing for differential expression

457 between the mock infected (cohort 2.3) and the SARS-CoV-2 Delta infected (cohort 2.1) mice
458 showed that of the 16,388 investigated genes, 1,103 genes were significantly up-regulated (log_2FC
459 >2, FDR <0.05) and 80 genes were significantly down-regulated (log_2FC <-2, FDR <0.05) (Figure 5B).
460 Heatmaps visualising the log CPM of each the top 20 up- and down-regulated genes after sorting by
461 FDR (Figure 5C, D) again found the brains of each cohort to cluster together; this is particularly
462 stringent for the 20 genes that were most significantly upregulated with infection (Figure 5C).
463 Subsequent pathway enrichment analysis, performed with GSEA and using both the GO and the
464 KEGG databases, showed on the one hand a positive enrichment of pathways involved in the
465 response to virus, defence to bacterium, inflammation, and immune response, on the other hand a
466 negative enrichment of pathways associated with synapses and behavioural defence/fear response
467 (Figure 6; Supplemental Figure S6).

468 To understand the molecular mechanisms underpinning the neuroinflammation, leukocyte
469 recruitment, and possible effects on the BBB and blood vessels, GSEA (with the GO database) was
470 used to gain further context of differentially expressed genes. With regards to inflammation, we saw
471 an enrichment of pathways associated with interferon type I and II, interleukin-1β (IL-1β), cytokines,
472 chemokines, tumour necrosis factor (TNF), and inflammasome (Figure 7A), consistent with an
473 inflammatory environment in the infected brains (cohort 2.1). Enrichment of pathways associated
474 with leukocytes adhesion to the vascular wall, migration, and chemotaxis was also seen, consistent
475 with active recruitment of leukocytes into the brain (Figure 7B, C), supporting our *in situ*
476 observations. Several enriched pathways related to leukocyte activity and the immune response
477 were identified (Figure 7D), indicating that the recruited leukocytes are part of a tissue response
478 directed against the virus. Further investigation revealed the enrichment of pathways associated
479 with different leukocyte subtypes, such as lymphocytes (CD4+ and CD8+ T cells, B cells, natural killer
480 cells), monocytes/macrophages, and neutrophils (all present in the (peri)vascular infiltrates
481 observed in infected brains; Supplemental Figure S4) which were mostly associated with leukocyte
482 activity, proliferation/differentiation, and migration/chemotaxis (Supplemental Figure S7). In

483 addition, the enrichment of pathways involved in leukocyte mediated cytotoxicity, cell killing,
484 degranulation, phagocytosis, respiratory burst, and reactive oxygen species suggests that leukocyte
485 recruitment is accompanied by activation (Supplemental Figure S7D). Interestingly, several pathways
486 associated with cell death were enriched, such as apoptotic process (including lymphocyte (T and B
487 cell) and neutrophil apoptotic process) and necroptotic process (Supplemental Figure S5D), a finding
488 in line with the leukocyte apoptosis detected *in situ* (Supplemental Figure S5A-C). Focusing on the
489 blood vessels and the BBB, our data revealed a positive enrichment of pathways associated with
490 angiogenesis/vascular development, endothelial cell migration and apoptotic process, smooth
491 muscle cell proliferation and apoptotic process, haemostasis, platelet activation/aggregation, blood
492 coagulation, fibrinolysis, and tight junction assembly; however, the morphological examination of
493 the blood vessels did not provide any evidence that the listed processes were pursued at
494 translational level and completed towards structural alterations. Interestingly, two pathways related
495 to cell junction were negatively enriched (positive regulation of cell junction assembly, and protein
496 localisation to cell junction) (Figure 7C), suggesting possible subtle structural changes of the
497 intercellular junctions. Investigation of the pathway enrichment analysis with the KEGG database
498 revealed similar findings as those identified with GO database (Supplemental Figure S8).

499 Based on the observed morphological changes, and from the insights offered by the
500 pathway analysis, we narrowed our investigation further and targeted several sets of genes which
501 we considered to be of interest, namely: 1) inflammatory mediators; 2) leukocyte recruitment
502 factors; 3) BBB key components/factors. Our data confirmed the presence of an inflammatory
503 environment in the infected brains, based on the significant upregulation (log_2FC >2 and FDR <0.05)
504 of cytokine and cytokine receptor genes (such as interleukins, chemokines, interferons, and TNF
505 super family), complement components and receptors, and prostaglandin synthase (Supplemental
506 Figure S9A, Supplemental Table S5). Regarding the recruitment of leukocytes, our data showed
507 significant upregulation of genes involved in different steps of this process [56, 81], such as capture
508 (*Vcam1*), rolling (*Selp*, *Sele*), arrest and adhesion (*Icam1*, *Vcam1*), polarisation (*Icam1*), crawling

509 against the blood flow (*Icam1*), migration across the endothelial barrier (*Cxcl10*, *Ccl2*, *Ccr7*), sojourn
510 in the perivascular space (*Mmp19*), and migration across the parenchymal barrier (*Timp1*, *Ccl2*,
511 *Tnfrsf1a*, *C3*) (Supplemental Figure S9B, Supplemental Table S5). For key factors of the BBB, we only
512 found angiopoietin 2 (Ang2) to be significantly upregulated. However, Ang2 mRNA and protein have
513 been described to be associated with BBB breakdown and increased permeability [94–96]. The other
514 genes investigated showed no significant up- or downregulation (Supplemental Table S5).
515
516

517 ## Discussion

518 The present study investigated the role of the blood vessels in SARS-CoV-2 infection of the brain in
519 the K18-hACE-2 mouse model. Intranasal challenge of K18-hACE-2 mice with SARS-CoV-2 VOC
520 proceeds to widespread infection of the brain in a large proportion of infected animals, most likely
521 via the olfactory route [25–27, 35, 40, 97]. Infection is often associated with a mild vessel-centred
522 inflammatory response and microgliosis [25–27, 35, 36, 38]. The former was a focus of the present
523 work, with special emphasis on leukocyte recruitment, integrity of the vascular wall, and
524 maintenance of BBB function. Combining morphological approaches and RNA sequencing analyses,
525 we confirmed that the infiltrating leukocytes (i.e. monocytes/macrophages, T cells, and neutrophils)
526 accumulate in the perivascular space of post-capillary venules, from which some appear to migrate
527 into the adjacent neuroparenchyma. The leukocytes emigrate from and then aggregate around the
528 vessel wall without any structural damage to the vessel. Also, there was no evidence of viral
529 infection of cells forming the vessel walls. This suggests that, while recruited to the brain, the
530 leukocytes did not target the blood vessels.

531 Given that SARS-CoV-2 infects neurons while sparing the blood vessels, activation of a
532 pathway originating in the neuroparenchyma and leading to functional activation of cerebral blood
533 vessels as well as recruitment of leukocytes into the perivascular space and beyond can be
534 postulated. One suitable candidate is the IL-1β pathway, involving microglia, astrocytes, and

535 endothelial cells. Under normal conditions, astrocytes produce Sonic hedgehog (SHH) which binds its
536 receptor on BBB endothelial cells and inhibits Patched-1 (Ptch1), leading to the activation of the
537 Smoothened (Smo)- Gli-1 signalling pathway, which maintains BBB integrity. In addition, the SHH
538 pathway limits the expression of inflammatory mediators by BBB endothelial cells and mediators of
539 leukocyte adhesion and migration [88, 98]. Activation of microglial cells leads to the release of IL-1β
540 which exerts both a direct and an indirect effect on the BBB. Indeed, IL-1β can downregulate tight
541 junction proteins, resulting in increased BBB permeability. IL-1β also interacts with astrocytes,
542 leading to the production of VEGF (which can apparently induce BBB disruption) and the suppression
543 of SHH [88, 99]. The latter leads to inhibition of the Smo-Gli-1 signalling pathway, resulting in
544 reduced tight junction protein levels and disruption of the BBB. In addition, IL-1β stimulates the
545 production of inflammatory chemokines by astrocytes, such as CXCL2, CCL2, and CCL20, causing the
546 recruitment of leukocytes [88]. Therefore, activation of the IL-1β signalling pathway would have two
547 important consequences, the recruitment of leukocytes, and increased permeability of the BBB. In
548 the present study, we found *Il-1*β, *Cxcl2*, and *Ccl2* significantly up-regulated in infected brains,
549 suggesting that the IL-1 β pathway could underly or at least contribute to the observed leukocyte
550 recruitment. This is supported by the fact that SARS-CoV-2 infection of the brain in h18-hACE2 mice
551 is accompanied by microglial activation [25, 26, 35]. Leukocyte migration across the BBB is a two-
552 step process that occurs at the level of post-capillary venules (Ineichen et al. 2022). First, the
553 leukocytes cross the endothelial layer and its associated basement membrane and accumulate in the
554 perivascular space. This event is mediated by different molecules involved in the capture, rolling,
555 arrest, adhesion, and migration of the leukocytes, such as VCAM-1, E/P-selectin, ACKR1, ICAM-1,
556 ICAM-2, CCR7, CCR8, CCL2, CXCL10, CD99L2, and TNFR1 [56, 81]. The present study detected
557 significantly higher transcription levels for several of these molecules (*Cxcl10*, *Ccl2*, *Icam1*, *Vcam1*,
558 *Selp*, *Sele*, *Ccr7*) in the SARS-CoV-2 infected brains, consistent with leukocyte recruitment into the
559 brain. Two routes, transcellular and paracellular, have been reported as mechanisms of passage
560 through the endothelial layer [81, 100–102]. In the present study, possibly because the main

561 recruitment process had already come to a close by the time of euthanasia, at 6-8 dpi, the
562 ultrastructural examination caught only rare leukocytes in the process of diapedesis. Therefore, we
563 were not able to determine which route was taken. Indeed, we detected structurally intact
564 intercellular junctions immediately adjacent to migrating (or migrated) leukocytes, but cannot
565 determine whether this reflects paracellular migration, or a previous transcellular migration.
566 Interestingly, T cells can enter the perivascular space before being activated, and remain there.
567 Activation would then confer their ability to migrate into the neuroparenchyma [56]. For migration
568 in the neuroparenchyma, the leukocytes need to cross the layer formed by the AEF and the
569 associated parenchymal basement membrane; this also requires a specific set of molecules [56], and
570 indeed, some of these were also significantly upregulated in infected brains (Ccl2, Tnfrsf1a, C3).
571 However, TIMP-1, a tissue inhibitor of matrix metalloproteinase, was also found to be
572 transcriptionally upregulated; the latter has been reported to inhibit leukocyte migration from the
573 perivascular space into the neuroparenchyma [56]. We suspect that in the present study, both
574 factors could have contributed to retaining most leukocytes in the perivascular spaces. The presence
575 of a few leukocytes (T cells, neutrophils and macrophages) in the neuroparenchyma would then
576 suggest some degree of activation as well as the presence of a chemotactic gradient; the nature and
577 origin of the latter, activated glial cells, astrocytes, or infected neurons, remain to be elucidated.
578 However, the fact that neuronal infection is associated with microglial activation in the SARS-CoV-2
579 infected mouse brains [25, 26, 35] indicates that infected neurons might be the primary trigger of
580 the inflammatory response, leading to activation of the microglia and the IL-1β signalling pathway.
581 Evidence of BBB disruption has been reported in human COVID-19 patients by various
582 approaches [103–106]. Using the mouse adapted SARS-CoV-2 MA10, two recent studies in mice also
583 indicated that SARS-CoV-2 infection of the lungs is associated with BBB disruption, and
584 demonstrated a potential role of the Wnt/β-catenin signalling pathway and caveolin-1 [107, 108]. In
585 addition, a study using an airway-on-a-chip model showed that SARS-CoV-2 infection altered the
586 expression of claudin 5, a major component of tight junctions [109]. Besides the IL-1β and Smo-Gli-1

587 signalling pathway [88], a mechanism downstream of CCL2 action on endothelial cells has also been
588 implicated in the increase of BBB permeability. Indeed, using *in vivo* and *in vitro* models, CCL2 has
589 been shown to increase endothelial permeability by causing phosphorylation and redistribution of
590 the tight junction proteins ZO-1, ZO-2, occludin, and claudin 5 [110–112]. In our study, investigation
591 of claudin 5 expression at light microscopical levels, and of intercellular junctions by TEM, and the
592 transcription of selected tight junction protein genes (*Ocln*, *Cldn1*, *Cldn3*, *Cldn5*, *Cldn12*, *Tjp1*, *Tjp2*,
593 *Tjp3*), as well as *Shh*, *Ptch1*, and *Smo* from the IL-1β and Smo-Gli-1 pathway, revealed no clear
594 differences in the infected brains compared to the controls. However, several findings suggest that
595 the BBB is disrupted to some degree in the brain of infected mice. First, in some vessels, associated
596 or not with a (peri)vascular infiltrate, we found evidence of increased glycogen accumulation in AEF.
597 Using a mouse model for cortical infarct, a study reported that increased glycogen in AEF was one of
598 the ultrastructural features associated with BBB disruption in affected brains [59]. Second, pathway
599 enrichment analysis showed the negative enrichment of two pathways associated with intercellular
600 junction, namely: positive regulation of cell junction assembly, protein localization of cell junction.
601 This could indicate that alterations of intercellular junctions have taken place at protein rather than
602 transcriptional level, as suggested before [110–112]. Further evidence of possible alterations of the
603 BBB comes from the finding that *Ang2*, which has been associated with BBB breakdown and
604 increased permeability [94–96], was significantly upregulated in infected brains.

605 We have previously described and now confirmed the presence of apoptotic debris/cells
606 both among the perivascular infiltrates and in the neuroparenchyma [26]. The ultrastructural
607 investigation supports that these are apoptotic leukocytes including phagocytised remnants of
608 neutrophils [113]. In line with this, our transcriptome analysis detected enrichment of pathways
609 associated with leukocyte (T and B cells, neutrophils) apoptosis, and we found *Fas* and *Fasl* to be
610 significantly upregulated, suggesting that these could induce the apoptosis at least of the T cells, also
611 to limit the inflammatory process [114], whereas neutrophil apoptosis might be a physiological, end
612 of life process [115].

613 The present study utilised bulk RNA sequencing, therefore transcriptomic signals could not
614 be interpreted at a single-cell level which would provide further insights into our findings of the
615 heterogeneity of transcriptomic responses across the many cell types. However, it provides a
616 detailed general picture of neuroinflammation in the course of a neurotropic but not overtly
617 neuropathic virus infection. Attempts to explain the pathomechanisms at play in this scenario are
618 based on knowledge gained from experimental autoimmune encephalomyelitis (EAE) [56, 81], a
619 model of inflammatory demyelinating disease and in particular multiple sclerosis [116], with similar
620 pathomechanisms as the Theiler's murine encephalitis model [117, 118]. The striking similarities
621 with regards to inflammatory environment, leukocyte recruitment and activation as well as BBB
622 (dys)function highlighted by the results of our transcriptomic analysis suggest that different triggers
623 and pathological processes in the brain share mediating molecular pathways and hence the principal
624 tissue response. Further studies are now warranted to pinpoint the primary insult that triggers the
625 observed processes in SARS-CoV-2 infection of the brain.
626

627 ## Conclusions

628 In conclusion, combining morphological and molecular analyses, our study shows that intranasal
629 infection of K18-hACE2 mice with different SARS-CoV-2 strains is associated with leukocyte
630 recruitment into the brain without damage to the blood vessels. There is no evidence that SARS-
631 CoV-2 targets the cerebral blood vessels, leading us to hypothesise that the neuroinflammation is
632 initiated by the infected neurons and carried by activated glial cells. Taken together these findings
633 could help understand the brain reaction to neuronal infection with viruses that are not overtly
634 cytopathic.
635
636

637 ## List of abbreviations

638 ACE2: angiotensin-converting enzyme 2

639 AEF: astrocytic endfeet

640 ANG2: angiopoietin 2

641 A-SMA: alpha smooth muscle actin

642 BBB: blood-brain barrier

643 BP: biological process

644 CNS: central nervous system

645 DPI: days post infection

646 FDR: false discovery rate

647 GA: glutaraldehyde

648 GO: gene ontology

649 GSEA: gene set enrichment analysis

650 hACE2: human angiotensin-converting enzyme 2

651 HE: haematoxylin and eosin

652 IHC: immunohistochemistry

653 Immune-EM: immune electron microscopy

654 IL-1β: interleukin-1β

655 KEGG: Kyoto encyclopedia of genes and genomes

656 Log_2 CPM: log_2-transformed counts per million

657 Log_2FC: log_2 fold change

658 LM: light microscopy

659 MOI: multiplicity of infection

660 NES: normalised enrichment score

661 NBF: neutral buffered formalin

662 NP: nucleocapsid protein

663 PBS: phosphate buffered saline

664 PCA: principal component analysis

665 PDGFR-β: platelet-derived growth factor receptor beta

666 PECAM-1: platelet endothelial cell adhesion molecule 1

667 PFU: plaque-forming unit

668 Ptch1: patched-1

669 RT: room temperature

670 RT-qPCR: reverse transcription quantitative real-time PCR

671 SARS-CoV-2: severe acute respiratory syndrome coronavirus 2

672 SHH: sonic hedgehog

673 Smo: smoothened

674 SPF: specific-pathogen free

675 TEM: transmission electron microscopy

676 TNF: tumour necrosis factor

677 VOC: variant of concern

678

679

680 Declarations

681 **Ethics approval and consent to participate**

682 Animal work was approved by the local University of Liverpool Animal Welfare and Ethical Review
683 Body and performed under UK Home Office Project Licence PP4715265. It was undertaken in
684 accordance with locally approved risk assessments and standard operating procedures.

685

686 **Consent for publication**

687 Not applicable.

688

Availability of data and materials

Sequencing data has been deposited on Short Read Archive (SRA) under the BioProject: PRJNA1220666.

Competing interests

The authors declare that they have no competing interests.

Funding

This work was funded by the European Union's Horizon Europe Research and Innovation Programme under grant agreement No 101057553 and the Swiss State Secretariat for Education, Research and Innovation (SERI) under contract number 22.00094.

Authors' contribution

AK (Anja Kipar), JPS, FS, UH, GB: conception and design of the project. SDN, BH, RPR, AK (Adam Kirby), PS, EHB: methodology. PS, EGB, AK (Adam Kirby), JPS: in vivo experimental work. GB: in vitro experimental work. SDN, RPR, PS, EGB, BH, AK (Adam Kirby): data collection. SDN, RPR, UH: data analysis. SDN, AK: writing of the original draft. SDB, AK (Anja Kipar), RPR, JPS, GB, UH, FS: review and editing. AK (Anja Kipar), JPS, GB: funding acquisition. AK: supervision of the project. All authors read and approved the manuscript.

Acknowledgements

We are grateful to the technical staff in the Histology Laboratory, Institute of Veterinary Pathology, Vetsuisse Faculty, University of Zurich (IVPZ), for excellent technical support.

References

1. Milross L, Majo J, Cooper N, Kaye PM, Bayraktar O, Filby A, Fisher AJ. Post-mortem lung tissue: the fossil record of the pathophysiology and immunopathology of severe COVID-19. The Lancet Respiratory Medicine. 2022;10:95–106. doi:10.1016/S2213-2600(21)00408-2.
2. Monje M, Iwasaki A. The neurobiology of long COVID. Neuron 2022. doi:10.1016/j.neuron.2022.10.006.
3. Mehandru S, Merad M. Pathological sequelae of long-haul COVID. Nat Immunol. 2022;23:194–202. doi:10.1038/s41590-021-01104-y.
4. Chou SH-Y, Beghi E, Helbok R, Moro E, Sampson J, Altamirano V, et al. Global incidence of neurological manifestations among patients hospitalized with COVID-19-A report for the GCS-NeuroCOVID Consortium and the ENERGY Consortium. JAMA Netw Open. 2021;4:e2112131. doi:10.1001/jamanetworkopen.2021.12131.
5. Ross Russell AL, Hardwick M, Jeyanantham A, White LM, Deb S, Burnside G, et al. Spectrum, risk factors and outcomes of neurological and psychiatric complications of COVID-19: a UK-wide cross-sectional surveillance study. Brain Commun. 2021;3:fcab168. doi:10.1093/braincomms/fcab168.
6. Khedr EM, Abo-Elfetoh N, Deaf E, Hassan HM, Amin MT, Soliman RK, et al. Surveillance study of acute neurological manifestations among 439 Egyptian patients with COVID-19 in Assiut and Aswan university hospitals. Neuroepidemiology. 2021;55:109–18. doi:10.1159/000513647.
7. Meinhardt J, Streit S, Dittmayer C, Manitius RV, Radbruch H, Heppner FL. The neurobiology of SARS-CoV-2 infection. Nat Rev Neurosci. 2024;25:30–42. doi:10.1038/s41583-023-00769-8.
8. Lemogne C, Gouraud C, Pitron V, Ranque B. Why the hypothesis of psychological mechanisms in long COVID is worth considering. J Psychosom Res. 2023;165:111135. doi:10.1016/j.jpsychores.2022.111135.
9. Liira H, Garner P, Malmivaara A, Kanerva M, Kvarnström K, Sainio M, et al. Prognosis of patients with post-Covid-19 condition: Prospective cohort cluster analysis at one year. J Psychosom Res. 2024;182:111808. doi:10.1016/j.jpsychores.2024.111808.
10. Saunders C, Sperling S, Bendstrup E. A new paradigm is needed to explain long COVID. Lancet Respir Med. 2023;11:e12-e13. doi:10.1016/S2213-2600(22)00501-X.
11. Mukerji SS, Solomon IH. What can we learn from brain autopsies in COVID-19? Neurosci Lett. 2021;742:135528. doi:10.1016/j.neulet.2020.135528.
12. Solomon IH, Singh A, Folkerth RD, Mukerji SS. What can we still learn from brain autopsies in COVID-19? Semin Neurol. 2023;43:195–204. doi:10.1055/s-0043-1767716.
13. Matschke J, Lütgehetmann M, Hagel C, Sperhake JP, Schröder AS, Edler C, et al. Neuropathology of patients with COVID-19 in Germany: a post-mortem case series. The Lancet Neurology. 2020;19:919–29. doi:10.1016/S1474-4422(20)30308-2.
14. Bocci M, Oudenaarden C, Sàenz-Sardà X, Simrén J, Edén A, Sjölund J, et al. Infection of brain pericytes underlying neuropathology of COVID-19 patients. Int J Mol Sci 2021. doi:10.3390/ijms222111622.
15. Agrawal S, Farfel JM, Arfanakis K, Al-Harthi L, Shull T, Teppen TL, et al. Brain autopsies of critically ill COVID-19 patients demonstrate heterogeneous profile of acute vascular injury, inflammation and age-linked chronic brain diseases. Acta Neuropathol Commun. 2022;10:186. doi:10.1186/s40478-022-01493-7.
16. Puelles VG, Lütgehetmann M, Lindenmeyer MT, Sperhake JP, Wong MN, Allweiss L, et al. Multiorgan and renal tropism of SARS-CoV-2. N Engl J Med. 2020;383:590–2. doi:10.1056/NEJMc2011400.

758 17. Deigendesch N, Sironi L, Kutza M, Wischnewski S, Fuchs V, Hench J, et al. Correlates of critical
759 illness-related encephalopathy predominate postmortem COVID-19 neuropathology. Acta
760 Neuropathol. 2020;140:583–6. doi:10.1007/s00401-020-02213-y.
761 18. Meinhardt J, Radke J, Dittmayer C, Franz J, Thomas C, Mothes R, et al. Olfactory transmucosal
762 SARS-CoV-2 invasion as a port of central nervous system entry in individuals with COVID-19. Nat
763 Neurosci. 2021;24:168–75. doi:10.1038/s41593-020-00758-5.
764 19. Fabbri VP, Riefolo M, Lazzarotto T, Gabrielli L, Cenacchi G, Gallo C, et al. COVID-19 and the brain:
765 The neuropathological Italian experience on 33 adult autopsies. Biomolecules 2022.
766 doi:10.3390/biom12050629.
767 20. Stein SR, Ramelli SC, Grazioli A, Chung J-Y, Singh M, Yinda CK, et al. SARS-CoV-2 infection and
768 persistence in the human body and brain at autopsy. Nature. 2022;612:758–63.
769 doi:10.1038/s41586-022-05542-y.
770 21. Gray-Rodriguez S, Jensen MP, Otero-Jimenez M, Hanley B, Swann OC, Ward PA, et al.
771 Multisystem screening reveals SARS-CoV-2 in neurons of the myenteric plexus and in
772 megakaryocytes. J Pathol. 2022;257:198–217. doi:10.1002/path.5878.
773 22. Andrews MG, Mukhtar T, Eze UC, Simoneau CR, Ross J, Parikshak N, et al. Tropism of SARS-CoV-
774 2 for human cortical astrocytes. Proc Natl Acad Sci U S A. 2022;119:e2122236119.
775 doi:10.1073/pnas.2122236119.
776 23. Crunfli F, Carregari VC, Veras FP, Silva LS, Nogueira MH, Antunes ASLM, et al. Morphological,
777 cellular, and molecular basis of brain infection in COVID-19 patients. Proc Natl Acad Sci U S A.
778 2022;119:e2200960119. doi:10.1073/pnas.2200960119.
779 24. McCray PB, Pewe L, Wohlford-Lenane C, Hickey M, Manzel L, Shi L, et al. Lethal infection of K18-
780 hACE2 mice infected with severe acute respiratory syndrome coronavirus. J Virol. 2007;81:813–
781 21. doi:10.1128/JVI.02012-06.
782 25. Carossino M, Kenney D, O'Connell AK, Montanaro P, Tseng AE, Gertje HP, et al. Fatal
783 neurodissemination and SARS-CoV-2 tropism in K18-hACE2 mice is only partially dependent on
784 hACE2 expression. Viruses 2022. doi:10.3390/v14030535.
785 26. Seehusen F, Clark JJ, Sharma P, Bentley EG, Kirby A, Subramaniam K, et al. Neuroinvasion and
786 neurotropism by SARS-CoV-2 variants in the K18-hACE2 mouse. Viruses 2022.
787 doi:10.3390/v14051020.
788 27. Kumari P, Rothan HA, Natekar JP, Stone S, Pathak H, Strate PG, et al. Neuroinvasion and
789 encephalitis following intranasal inoculation of SARS-CoV-2 in K18-hACE2 mice. Viruses 2021.
790 doi:10.3390/v13010132.
791 28. Song E, Zhang C, Israelow B, Lu-Culligan A, Prado AV, Skriabine S, et al. Neuroinvasion of SARS-
792 CoV-2 in human and mouse brain. J Exp Med 2021. doi:10.1084/jem.20202135.
793 29. Hassan AO, Case JB, Winkler ES, Thackray LB, Kafai NM, Bailey AL, et al. A SARS-CoV-2 infection
794 model in mice demonstrates protection by neutralizing antibodies. Cell. 2020;182:744-753.e4.
795 doi:10.1016/j.cell.2020.06.011.
796 30. Fumagalli V, Ravà M, Marotta D, Di Lucia P, Laura C, Sala E, et al. Administration of aerosolized
797 SARS-CoV-2 to K18-hACE2 mice uncouples respiratory infection from fatal neuroinvasion. Sci
798 Immunol. 2022;7:eabl9929. doi:10.1126/sciimmunol.abl9929.
799 31. Winkler ES, Bailey AL, Kafai NM, Nair S, McCune BT, Yu J, et al. SARS-CoV-2 infection of human
800 ACE2-transgenic mice causes severe lung inflammation and impaired function. Nat Immunol.
801 2020;21:1327–35. doi:10.1038/s41590-020-0778-2.
802 32. Gan ES, Syenina A, Linster M, Ng B, Zhang SL, Watanabe S, et al. A mouse model of lethal
803 respiratory dysfunction for SARS-CoV-2 infection. Antiviral Res. 2021;193:105138.
804 doi:10.1016/j.antiviral.2021.105138.

805 33. Olivarria GM, Cheng Y, Furman S, Pachow C, Hohsfield LA, Smith-Geater C, et al. Microglia do
806 not restrict SARS-CoV-2 replication following infection of the central nervous system of K18-
807 human ACE2 transgenic mice. J Virol. 2022;96:e0196921. doi:10.1128/jvi.01969-21.
808 34. Tarrés-Freixas F, Trinité B, Pons-Grífols A, Romero-Durana M, Riveira-Muñoz E, Ávila-Nieto C, et
809 al. Heterogeneous infectivity and pathogenesis of SARS-CoV-2 variants Beta, Delta and Omicron
810 in transgenic K18-hACE2 and wildtype mice. Front Microbiol. 2022;13:840757.
811 doi:10.3389/fmicb.2022.840757.
812 35. Vidal E, López-Figueroa C, Rodon J, Pérez M, Brustolin M, Cantero G, et al. Chronological brain
813 lesions after SARS-CoV-2 infection in hACE2-transgenic mice. Vet Pathol. 2022;59:613–26.
814 doi:10.1177/03009858211066841.
815 36. Yinda CK, Port JR, Bushmaker T, Offei Owusu I, Purushotham JN, Avanzato VA, et al. K18-hACE2
816 mice develop respiratory disease resembling severe COVID-19. PLoS Pathog. 2021;17:e1009195.
817 doi:10.1371/journal.ppat.1009195.
818 37. Zhang L, Zhou L, Bao L, Liu J, Zhu H, Lv Q, et al. SARS-CoV-2 crosses the blood-brain barrier
819 accompanied with basement membrane disruption without tight junctions alteration. Signal
820 Transduct Target Ther. 2021;6:337. doi:10.1038/s41392-021-00719-9.
821 38. Oladunni FS, Park J-G, Pino PA, Gonzalez O, Akhter A, Allué-Guardia A, et al. Lethality of SARS-
822 CoV-2 infection in K18 human angiotensin-converting enzyme 2 transgenic mice. Nat Commun.
823 2020;11:6122. doi:10.1038/s41467-020-19891-7.
824 39. Lee KS, Wong TY, Russ BP, Horspool AM, Miller OA, Rader NA, et al. SARS-CoV-2 Delta variant
825 induces enhanced pathology and inflammatory responses in K18-hACE2 mice. PLoS One.
826 2022;17:e0273430. doi:10.1371/journal.pone.0273430.
827 40. Yang J-H, Yang M-S, Kim D-M, Kim B, Tark D, Kang S-M, Lee G-H. Delta (B1.617.2) variant of
828 SARS-CoV-2 induces severe neurotropic patterns in K18-hACE2 mice. Scientific reports.
829 2023;13:3303. doi:10.1038/s41598-023-29909-x.
830 41. Sieracka J, Sieracki P, Kozera G, Szurowska E, Gulczyński J, Sobolewski P, et al. COVID-19 -
831 neuropathological point of view, pathobiology, and dilemmas after the first year of the
832 pandemic struggle. Folia Neuropathol. 2021;59:1–16. doi:10.5114/fn.2021.105128.
833 42. Chakravarty D, Das Sarma J. Murine-β-coronavirus-induced neuropathogenesis sheds light on
834 CNS pathobiology of SARS-CoV2. J Neurovirol. 2021;27:197–216. doi:10.1007/s13365-021-
835 00945-5.
836 43. Butowt R, Meunier N, Bryche B, Bartheld CS von. The olfactory nerve is not a likely route to
837 brain infection in COVID-19: a critical review of data from humans and animal models. Acta
838 Neuropathol. 2021;141:809–22. doi:10.1007/s00401-021-02314-2.
839 44. Martínez-Mármol R, Giordano-Santini R, Kaulich E, Cho A-N, Przybyla M, Riyadh MA, et al. SARS-
840 CoV-2 infection and viral fusogens cause neuronal and glial fusion that compromises neuronal
841 activity. Sci Adv. 2023;9:eadg2248. doi:10.1126/sciadv.adg2248.
842 45. Pinja K, Janika R, Tania Q, Ravi O, Saber SH, Shaker M, et al. SARS-CoV-2 infection in hiPSC-
843 derived neurons is cathepsin-dependent and causes accumulation of HIF1 and phosphorylated
844 tau; 2024.
845 46. Patterson EI, Prince T, Anderson ER, Casas-Sanchez A, Smith SL, Cansado-Utrilla C, et al.
846 Methods of inactivation of SARS-CoV-2 for downstream biological assays. J Infect Dis.
847 2020;222:1462–7. doi:10.1093/infdis/jiaa507.
848 47. Clark JJ, Penrice-Randal R, Sharma P, Dong X, Pennington SH, Marriott AE, et al. Sequential
849 infection with Influenza A virus followed by Severe Acute Respiratory Syndrome Coronavirus 2
850 (SARS-CoV-2) leads to more severe disease and encephalitis in a mouse model of COVID-19.
851 Viruses 2024. doi:10.3390/v16060863.

852 48. Cabrera LE, Jokiranta ST, Mäki S, Miettinen S, Kant R, Kareinen L, et al. The assembly of
853 neutrophil inflammasomes during COVID-19 is mediated by type I interferons. PLoS Pathog.
854 2024;20:e1012368. doi:10.1371/journal.ppat.1012368.
855 49. Kang Y, Hepojoki J, Maldonado RS, Mito T, Terzioglu M, Manninen T, et al. Ancestral allele of
856 DNA polymerase gamma modifies antiviral tolerance. Nature. 2024;628:844–53.
857 doi:10.1038/s41586-024-07260-z.
858 50. Winkler EA, Bell RD, Zlokovic BV. Pericyte-specific expression of PDGF beta receptor in mouse
859 models with normal and deficient PDGF beta receptor signaling. Mol Neurodegener. 2010;5:32.
860 doi:10.1186/1750-1326-5-32.
861 51. Hubbard JA, Hsu MS, Seldin MM, Binder DK. Expression of the astrocyte water channel
862 aquaporin-4 in the mouse brain. ASN Neuro 2015. doi:10.1177/1759091415605486.
863 52. Crouch EE, Doetsch F. FACS isolation of endothelial cells and pericytes from mouse brain
864 microregions. Nat Protoc. 2018;13:738–51. doi:10.1038/nprot.2017.158.
865 53. Grant RI, Hartmann DA, Underly RG, Berthiaume A-A, Bhat NR, Shih AY. Organizational hierarchy
866 and structural diversity of microvascular pericytes in adult mouse cortex. Journal of Cerebral
867 Blood Flow & Metabolism. 2019;39:411–25. doi:10.1177/0271678X17732229.
868 54. Greene C, Hanley N, Campbell M. Claudin-5: gatekeeper of neurological function. Fluids Barriers
869 CNS. 2019;16:3. doi:10.1186/s12987-019-0123-z.
870 55. Gautam J, Zhang X, Yao Y. The role of pericytic laminin in blood brain barrier integrity
871 maintenance. Scientific reports. 2016;6:36450. doi:10.1038/srep36450.
872 56. Ineichen BV, Okar SV, Proulx ST, Engelhardt B, Lassmann H, Reich DS. Perivascular spaces and
873 their role in neuroinflammation. Neuron. 2022;110:3566–81.
874 doi:10.1016/j.neuron.2022.10.024.
875 57. Nahirney PC, Tremblay M-E. Brain ultrastructure: putting the pieces together. Front Cell Dev
876 Biol. 2021;9:629503. doi:10.3389/fcell.2021.629503.
877 58. Krasemann S, Dittmayer C, Stillfried S von, Meinhardt J, Heinrich F, Hartmann K, et al. Assessing
878 and improving the validity of COVID-19 autopsy studies - A multicentre approach to establish
879 essential standards for immunohistochemical and ultrastructural analyses. EBioMedicine.
880 2022;83:104193. doi:10.1016/j.ebiom.2022.104193.
881 59. Nahirney PC, Reeson P, Brown CE. Ultrastructural analysis of blood-brain barrier breakdown in
882 the peri-infarct zone in young adult and aged mice. J Cereb Blood Flow Metab. 2016;36:413–25.
883 doi:10.1177/0271678X15608396.
884 60. Haley MJ, Lawrence CB. The blood-brain barrier after stroke: Structural studies and the role of
885 transcytotic vesicles. J Cereb Blood Flow Metab. 2017;37:456–70.
886 doi:10.1177/0271678X16629976.
887 61. Kajihara H, Tsutsumi E, Kinoshita A, Nakano J, Takagi K, Takeo S. Activated astrocytes with
888 glycogen accumulation in ischemic penumbra during the early stage of brain infarction:
889 immunohistochemical and electron microscopic studies. Brain Res. 2001;909:92–101.
890 doi:10.1016/s0006-8993(01)02640-3.
891 62. Sá-Pereira I, Brites D, Brito MA. Neurovascular unit: a focus on pericytes. Mol Neurobiol.
892 2012;45:327–47. doi:10.1007/s12035-012-8244-2.
893 63. Díaz-Castro B, Robel S, Mishra A. Astrocyte endfeet in brain function and pathology: Open
894 questions. Annu Rev Neurosci. 2023;46:101–21. doi:10.1146/annurev-neuro-091922-031205.
895 64. Hartmann DA, Coelho-Santos V, Shih AY. Pericyte control of blood flow across microvascular
896 zones in the central nervous system. Annu Rev Physiol. 2022;84:331–54. doi:10.1146/annurev-
897 physiol-061121-040127.

898 65. Gouveia-Freitas K, Bastos-Leite AJ. Perivascular spaces and brain waste clearance systems:
899 relevance for neurodegenerative and cerebrovascular pathology. Neuroradiology.
900 2021;63:1581–97. doi:10.1007/s00234-021-02718-7.
901 66. Ojha R, Jiang A, Mäntylä E, Quirin T, Modhira N, Witte R, et al. Dynamin independent
902 endocytosis is an alternative cell entry mechanism for multiple animal viruses. PLoS Pathog.
903 2024;20:e1012690. doi:10.1371/journal.ppat.1012690.
904 67. Chen S, Zhou Y, Chen Y, Gu J. fastp: an ultra-fast all-in-one FASTQ preprocessor. Bioinformatics.
905 2018;34:i884-i890. doi:10.1093/bioinformatics/bty560.
906 68. Patro R, Duggal G, Love MI, Irizarry RA, Kingsford C. Salmon provides fast and bias-aware
907 quantification of transcript expression. Nat Methods. 2017;14:417–9. doi:10.1038/nmeth.4197.
908 69. Soneson C, Love MI, Robinson MD. Differential analyses for RNA-seq: transcript-level estimates
909 improve gene-level inferences. F1000Res. 2015;4:1521. doi:10.12688/f1000research.7563.2.
910 70. R Core Team. R: A language and environment for statistical computing. Vienna, Austria: R
911 Foundation for Statistical Computing; 2024.
912 71. Chen Y, Chen L, Lun ATL, Baldoni PL, Smyth GK. edgeR v4: powerful differential analysis of
913 sequencing data with expanded functionality and improved support for small counts and larger
914 datasets. bioRxiv 2024. doi:10.1101/2024.01.21.576131.
915 72. Blighe Kevin, Lun Aaron. PCAtools: PCAtools: Everything Principal Components Analysis; 2024.
916 73. Kevin Blighe. EnhancedVolcano: Publication-ready volcano plots with enhanced colouring and
917 labeling: Bioconductor; 2024.
918 74. Kolde Raivo. pheatmap: Pretty heatmaps; 2018.
919 75. Xu S, Hu E, Cai Y, Xie Z, Luo X, Zhan L, et al. Using clusterProfiler to characterize multiomics data.
920 Nat Protoc. 2024;19:3292–320. doi:10.1038/s41596-024-01020-z.
921 76. Luo W, Brouwer C. Pathview: an R/Bioconductor package for pathway-based data integration
922 and visualization. Bioinformatics. 2013;29:1830–1. doi:10.1093/bioinformatics/btt285.
923 77. Cui A, Huang T, Li S, Ma A, Pérez JL, Sander C, et al. Dictionary of immune responses to cytokines
924 at single-cell resolution. Nature. 2024;625:377–84. doi:10.1038/s41586-023-06816-9.
925 78. Hughes CE, Nibbs RJB. A guide to chemokines and their receptors. FEBS J. 2018;285:2944–71.
926 doi:10.1111/febs.14466.
927 79. Haeggström JZ. Leukotriene biosynthetic enzymes as therapeutic targets. J Clin Invest.
928 2018;128:2680–90. doi:10.1172/JCI97945.
929 80. Ricciotti E, FitzGerald GA. Prostaglandins and inflammation. Arterioscler Thromb Vasc Biol.
930 2011;31:986–1000. doi:10.1161/ATVBAHA.110.207449.
931 81. Marchetti L, Engelhardt B. Immune cell trafficking across the blood-brain barrier in the absence
932 and presence of neuroinflammation. Vasc Biol. 2020;2:H1-H18. doi:10.1530/VB-19-0033.
933 82. Knox EG, Aburto MR, Clarke G, Cryan JF, O'Driscoll CM. The blood-brain barrier in aging and
934 neurodegeneration. Mol Psychiatry. 2022;27:2659–73. doi:10.1038/s41380-022-01511-z.
935 83. Zhao Z, Nelson AR, Betsholtz C, Zlokovic BV. Establishment and dysfunction of the blood-brain
936 barrier. Cell. 2015;163:1064–78. doi:10.1016/j.cell.2015.10.067.
937 84. Wareham LK, Baratta RO, Del Buono BJ, Schlumpf E, Calkins DJ. Collagen in the central nervous
938 system: contributions to neurodegeneration and promise as a therapeutic target. Mol
939 Neurodegener. 2024;19:11. doi:10.1186/s13024-024-00704-0.
940 85. Halder SK, Sapkota A, Milner R. The importance of laminin at the blood-brain barrier. Neural
941 Regen Res. 2023;18:2557–63. doi:10.4103/1673-5374.373677.
942 86. Ohno Y, Kunisawa N, Shimizu S. Emerging roles of astrocyte Kir4.1 channels in the pathogenesis
943 and treatment of brain diseases. Int J Mol Sci 2021. doi:10.3390/ijms221910236.
944 87. Bataveljić D, Nikolić L, Milosević M, Todorović N, Andjus PR. Changes in the astrocytic
945 aquaporin-4 and inwardly rectifying potassium channel expression in the brain of the

946 amyotrophic lateral sclerosis SOD1(G93A) rat model. Glia. 2012;60:1991–2003.
947 doi:10.1002/glia.22414.
948 88. Wang Y, Jin S, Sonobe Y, Cheng Y, Horiuchi H, Parajuli B, et al. Interleukin-1β induces blood-brain
949 barrier disruption by downregulating Sonic hedgehog in astrocytes. PLoS One. 2014;9:e110024.
950 doi:10.1371/journal.pone.0110024.
951 89. Rathnasinghe R, Strohmeier S, Amanat F, Gillespie VL, Krammer F, García-Sastre A, et al.
952 Comparison of transgenic and adenovirus hACE2 mouse models for SARS-CoV-2 infection.
953 Emerg Microbes Infect. 2020;9:2433–45. doi:10.1080/22221751.2020.1838955.
954 90. Mathiisen TM, Lehre KP, Danbolt NC, Ottersen OP. The perivascular astroglial sheath provides a
955 complete covering of the brain microvessels: an electron microscopic 3D reconstruction. Glia.
956 2010;58:1094–103. doi:10.1002/glia.20990.
957 91. Li J, Xu P, Hong Y, Xie Y, Peng M, Sun R, et al. Lipocalin-2-mediated astrocyte pyroptosis
958 promotes neuroinflammatory injury via NLRP3 inflammasome activation in cerebral
959 ischemia/reperfusion injury. J Neuroinflammation. 2023;20:148. doi:10.1186/s12974-023-
960 02819-5.
961 92. Jha MK, Lee S, Park DH, Kook H, Park K-G, Lee I-K, Suk K. Diverse functional roles of lipocalin-2 in
962 the central nervous system. Neurosci Biobehav Rev. 2015;49:135–56.
963 doi:10.1016/j.neubiorev.2014.12.006.
964 93. van Zuylen WJ, Garceau V, Idris A, Schroder K, Irvine KM, Lattin JE, et al. Macrophage activation
965 and differentiation signals regulate schlafen-4 gene expression: evidence for Schlafen-4 as a
966 modulator of myelopoiesis. PLoS One. 2011;6:e15723. doi:10.1371/journal.pone.0015723.
967 94. Nourhaghighi N, Teichert-Kuliszewska K, Davis J, Stewart DJ, Nag S. Altered expression of
968 angiopoietins during blood-brain barrier breakdown and angiogenesis. Lab Invest.
969 2003;83:1211–22. doi:10.1097/01.lab.0000082383.40635.fe.
970 95. Gurnik S, Devraj K, Macas J, Yamaji M, Starke J, Scholz A, et al. Angiopoietin-2-induced blood-
971 brain barrier compromise and increased stroke size are rescued by VE-PTP-dependent
972 restoration of Tie2 signaling. Acta Neuropathol. 2016;131:753–73. doi:10.1007/s00401-016-
973 1551-3.
974 96. Nag S, Papneja T, Venugopalan R, Stewart DJ. Increased angiopoietin2 expression is associated
975 with endothelial apoptosis and blood-brain barrier breakdown. Lab Invest. 2005;85:1189–98.
976 doi:10.1038/labinvest.3700325.
977 97. Zheng J, Wong L-YR, Li K, Verma AK, Ortiz ME, Wohlford-Lenane C, et al. COVID-19 treatments
978 and pathogenesis including anosmia in K18-hACE2 mice. Nature. 2021;589:603–7.
979 doi:10.1038/s41586-020-2943-z.
980 98. Alvarez JI, Dodelet-Devillers A, Kebir H, Ifergan I, Fabre PJ, Terouz S, et al. The Hedgehog
981 pathway promotes blood-brain barrier integrity and CNS immune quiescence. Science.
982 2011;334:1727–31. doi:10.1126/science.1206936.
983 99. Argaw AT, Zhang Y, Snyder BJ, Zhao M-L, Kopp N, Lee SC, et al. IL-1beta regulates blood-brain
984 barrier permeability via reactivation of the hypoxia-angiogenesis program. J Immunol.
985 2006;177:5574–84. doi:10.4049/jimmunol.177.8.5574.
986 100. Lossinsky AS, Shivers RR. Structural pathways for macromolecular and cellular transport across
987 the blood-brain barrier during inflammatory conditions. Review. Histol Histopathol.
988 2004;19:535–64. doi:10.14670/HH-19.535.
989 101. Erickson MA, Wilson ML, Banks WA. In vitro modeling of blood-brain barrier and interface
990 functions in neuroimmune communication. Fluids Barriers CNS. 2020;17:26.
991 doi:10.1186/s12987-020-00187-3.

992 102. Wolburg H, Wolburg-Buchholz K, Engelhardt B. Diapedesis of mononuclear cells across cerebral
993 venules during experimental autoimmune encephalomyelitis leaves tight junctions intact. Acta
994 Neuropathol. 2005;109:181–90. doi:10.1007/s00401-004-0928-x.
995 103. Bonetto V, Pasetto L, Lisi I, Carbonara M, Zangari R, Ferrari E, et al. Markers of blood-brain
996 barrier disruption increase early and persistently in COVID-19 patients with neurological
997 manifestations. Front Immunol. 2022;13:1070379. doi:10.3389/fimmu.2022.1070379.
998 104. Song H, Tomasevich A, Acheampong KK, Schaff DL, Shaffer SM, Dolle J-P, et al. Detection of
999 blood-brain barrier disruption in brains of patients with COVID-19, but no evidence of brain
1000 penetration by SARS-CoV-2. Acta Neuropathol. 2023;146:771–5. doi:10.1007/s00401-023-
1001 02624-7.
1002 105. Bellon M, Schweblin C, Lambeng N, Cherpillod P, Vazquez J, Lalive PH, et al. Cerebrospinal fluid
1003 features in Severe Acute Respiratory Syndrome Coronavirus 2 (SARS-CoV-2) reverse
1004 transcription polymerase chain reaction (RT-PCR) positive patients. Clin Infect Dis.
1005 2021;73:e3102-e3105. doi:10.1093/cid/ciaa1165.
1006 106. Greene C, Connolly R, Brennan D, Laffan A, O'Keeffe E, Zaporojan L, et al. Blood-brain barrier
1007 disruption and sustained systemic inflammation in individuals with long COVID-associated
1008 cognitive impairment. Nat Neurosci. 2024;27:421–32. doi:10.1038/s41593-024-01576-9.
1009 107. Trevino TN, Fogel AB, Otkiran G, Niladhuri SB, Sanborn MA, Class J, et al. Engineered Wnt7a
1010 ligands rescue blood-brain barrier and cognitive deficits in a COVID-19 mouse model. Brain.
1011 2024;147:1636–43. doi:10.1093/brain/awae031.
1012 108. Trevino TN, Almousawi AA, Robinson KF, Fogel AB, Class J, Minshall RD, et al. Caveolin-1
1013 mediates blood-brain barrier permeability, neuroinflammation, and cognitive impairment in
1014 SARS-CoV-2 infection. J Neuroimmunol. 2024;388:578309. doi:10.1016/j.jneuroim.2024.578309.
1015 109. Hashimoto R, Takahashi J, Shirakura K, Funatsu R, Kosugi K, Deguchi S, et al. SARS-CoV-2 disrupts
1016 respiratory vascular barriers by suppressing Claudin-5 expression. Sci Adv. 2022;8:eabo6783.
1017 doi:10.1126/sciadv.abo6783.
1018 110. Stamatovic SM, Dimitrijevic OB, Keep RF, Andjelkovic AV. Protein kinase Calpha-RhoA cross-talk
1019 in CCL2-induced alterations in brain endothelial permeability. J Biol Chem. 2006;281:8379–88.
1020 doi:10.1074/jbc.M513122200.
1021 111. Stamatovic SM, Keep RF, Kunkel SL, Andjelkovic AV. Potential role of MCP-1 in endothelial cell
1022 tight junction 'opening': signaling via Rho and Rho kinase. J Cell Sci. 2003;116:4615–28.
1023 doi:10.1242/jcs.00755.
1024 112. Stamatovic SM, Shakui P, Keep RF, Moore BB, Kunkel SL, van Rooijen N, Andjelkovic AV.
1025 Monocyte chemoattractant protein-1 regulation of blood-brain barrier permeability. J Cereb
1026 Blood Flow Metab. 2005;25:593–606. doi:10.1038/sj.jcbfm.9600055.
1027 113. Savill J, Smith J, Sarraf C, Ren Y, Abbott F, Rees A. Glomerular mesangial cells and inflammatory
1028 macrophages ingest neutrophils undergoing apoptosis. Kidney Int. 1992;42:924–36.
1029 doi:10.1038/ki.1992.369.
1030 114. Yamada A, Arakaki R, Saito M, Kudo Y, Ishimaru N. Dual role of Fas/FasL mediated signal in
1031 peripheral immune tolerance. Front Immunol. 2017;8:403. doi:10.3389/fimmu.2017.00403.
1032 115. Dejas L, Santoni K, Meunier E, Lamkanfi M. Regulated cell death in neutrophils: From apoptosis
1033 to NETosis and pyroptosis. Semin Immunol. 2023;70:101849. doi:10.1016/j.smim.2023.101849.
1034 116. Constantinescu CS, Farooqi N, O'Brien K, Gran B. Experimental autoimmune encephalomyelitis
1035 (EAE) as a model for multiple sclerosis (MS). Br J Pharmacol. 2011;164:1079–106.
1036 doi:10.1111/j.1476-5381.2011.01302.x.
1037 117. Howe CL, LaFrance-Corey RG, Goddery EN, Johnson RK, Mirchia K. Neuronal CCL2 expression
1038 drives inflammatory monocyte infiltration into the brain during acute virus infection. J
1039 Neuroinflammation. 2017;14:238. doi:10.1186/s12974-017-1015-2.

1040 118. Gerhauser I, Hansmann F, Ciurkiewicz M, Löscher W, Beineke A. Facets of Theiler's Murine
1041 Encephalomyelitis Virus-induced diseases: An update. Int J Mol Sci 2019.
1042 doi:10.3390/ijms20020448.
1043

1044

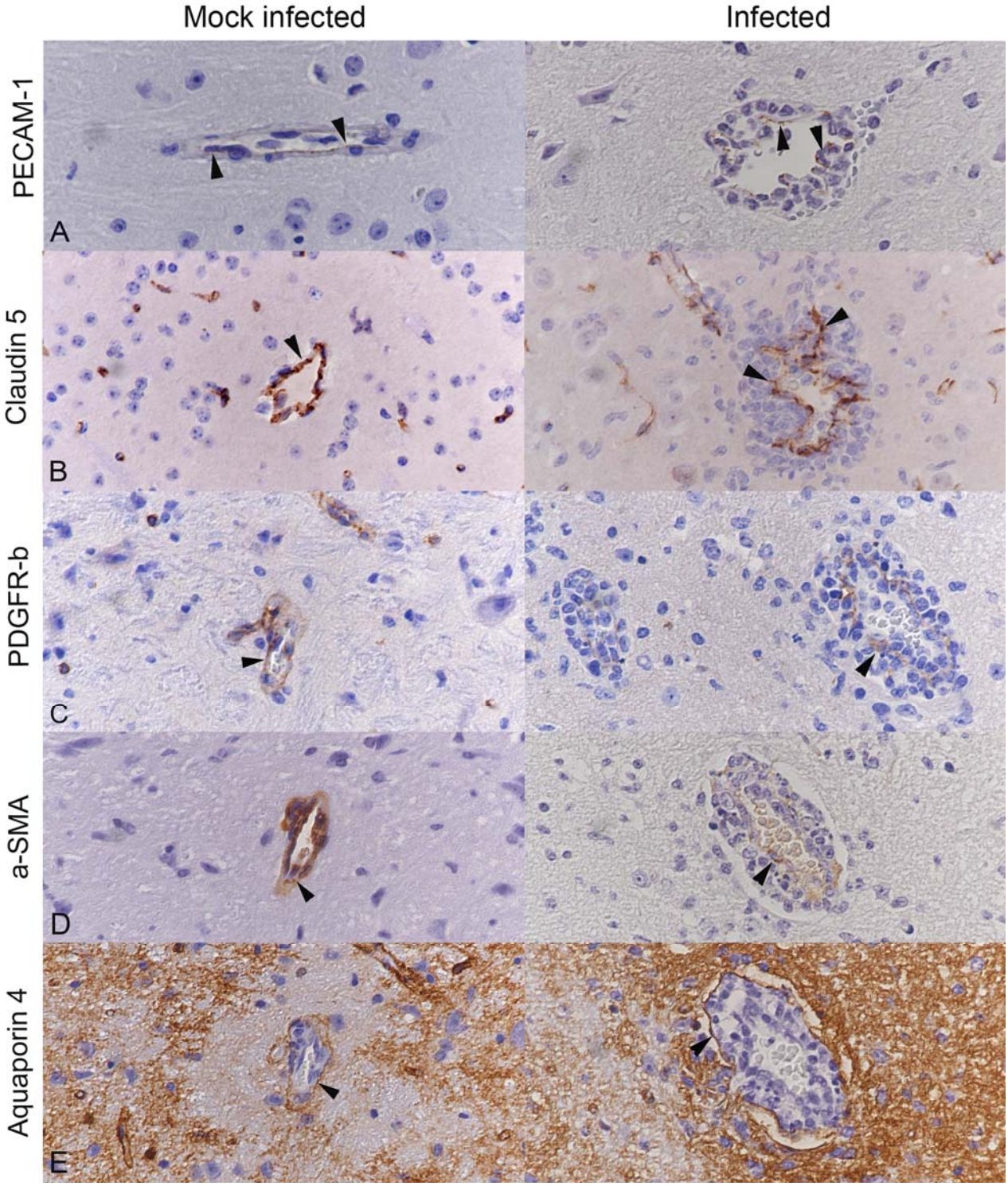

Figure 1. Structural key components of the blood-brain barrier are not damaged with (peri)vascular leukocyte infiltration. Brainstem of mock infected mice (left column; cohort 2.3) or mice infected with SARS-CoV-2 Delta at 10^2 PFU and euthanized at 7 dpi (right column; cohort 2.1). **A)** Endothelial cells (PECAM-1+; arrowheads) form a continuous layer (animals 2.1.4 and 2.3.2). **B)** Staining of the tight junction protein claudin 5 (arrowheads) confirms the integrity of the endothelial layer (animals 2.1.8 and 2.3.2). **C, D)** Staining of pericytes and leiomyocytes (C: PDGFR-β+; D: α-SMA+; arrowheads) highlights the integrity of the vascular wall (animals 2.1.4 and 2.3.1). **E)** Staining of astrocytic endfeet (aquaporin 4+) highlights that the infiltrating leukocytes

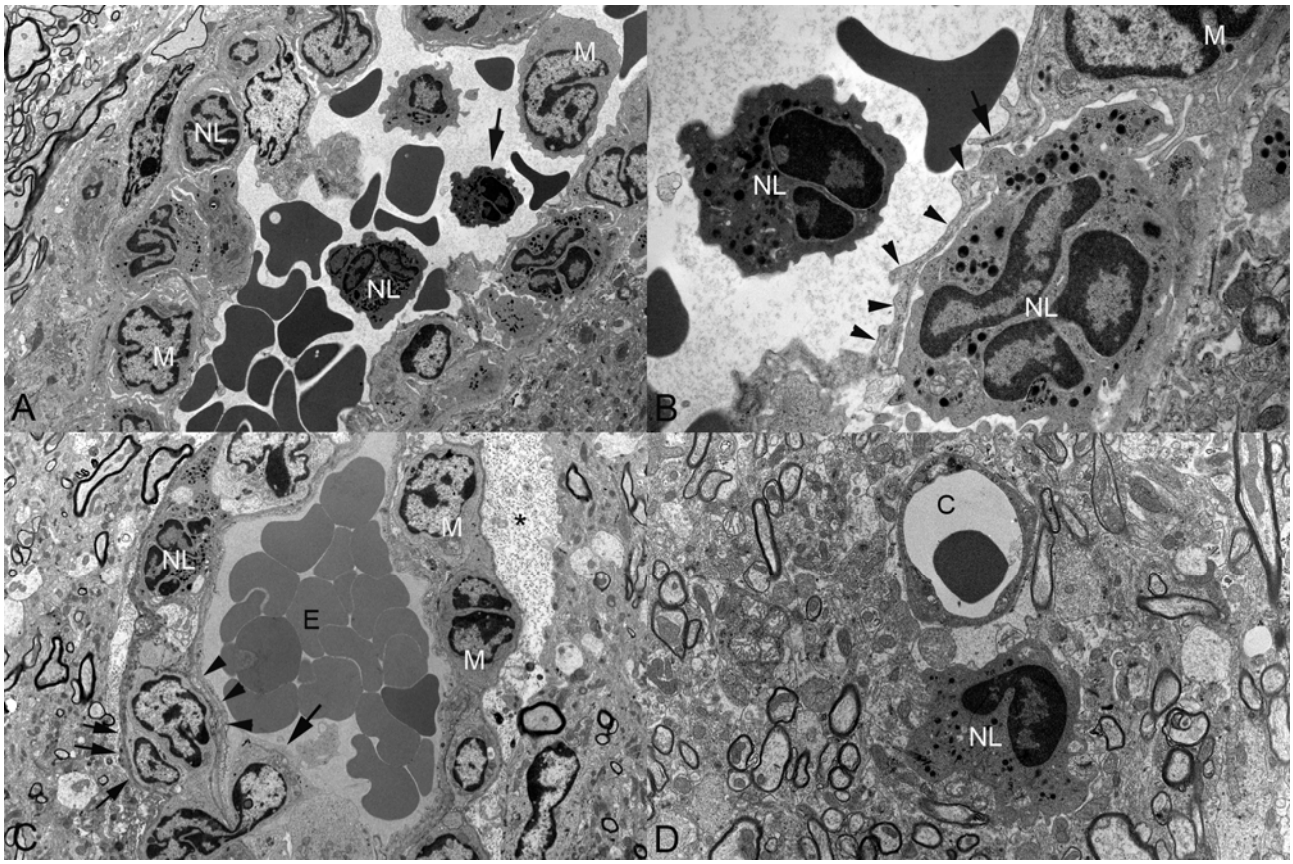

Figure 2. The (peri)vascular infiltrates are a consequence of leukocyte emigration without damage to the vascular wall. Brainstem, mice infected with SARS-CoV-2 Delta at 10^2 PFU (cohort 2.1) or 10^3 PFU (cohort 2.2) and euthanized at 6, 7, or 8 dpi. **A, B)** Animal 2.2.4. Post-capillary venule with accumulation of monocytes/macrophages (M) and neutrophilic leukocytes (NL) in the lumen and beneath the endothelial layer. The higher magnification (B; area indicated by the arrow in A) highlights a neutrophilic leukocyte and a monocyte/macrophage beneath the endothelial layer (arrowheads); the arrow points at an intact intercellular junction. **C)** Animal 2.1.4. Accumulation of monocytes/macrophages (M) and neutrophilic leukocytes (NL) in the perivascular space of a post-capillary venule. A leukocyte (likely a monocyte) is seen crossing the endothelial layer and its basement membrane (arrow). The vascular lumen is filled with erythrocytes (E). The astrocytic endfeet contain abundant finely granular electron-dense material (consistent with glycogen) (asterisk). Arrowheads: endothelial cells and associated basement membrane; small arrows: parenchymal basement membrane. **D)** Animal 2.1.1. Neutrophilic leukocyte (NL) in the neuroparenchyma immediately adjacent to a capillary (C). Transmission electron microscopy.

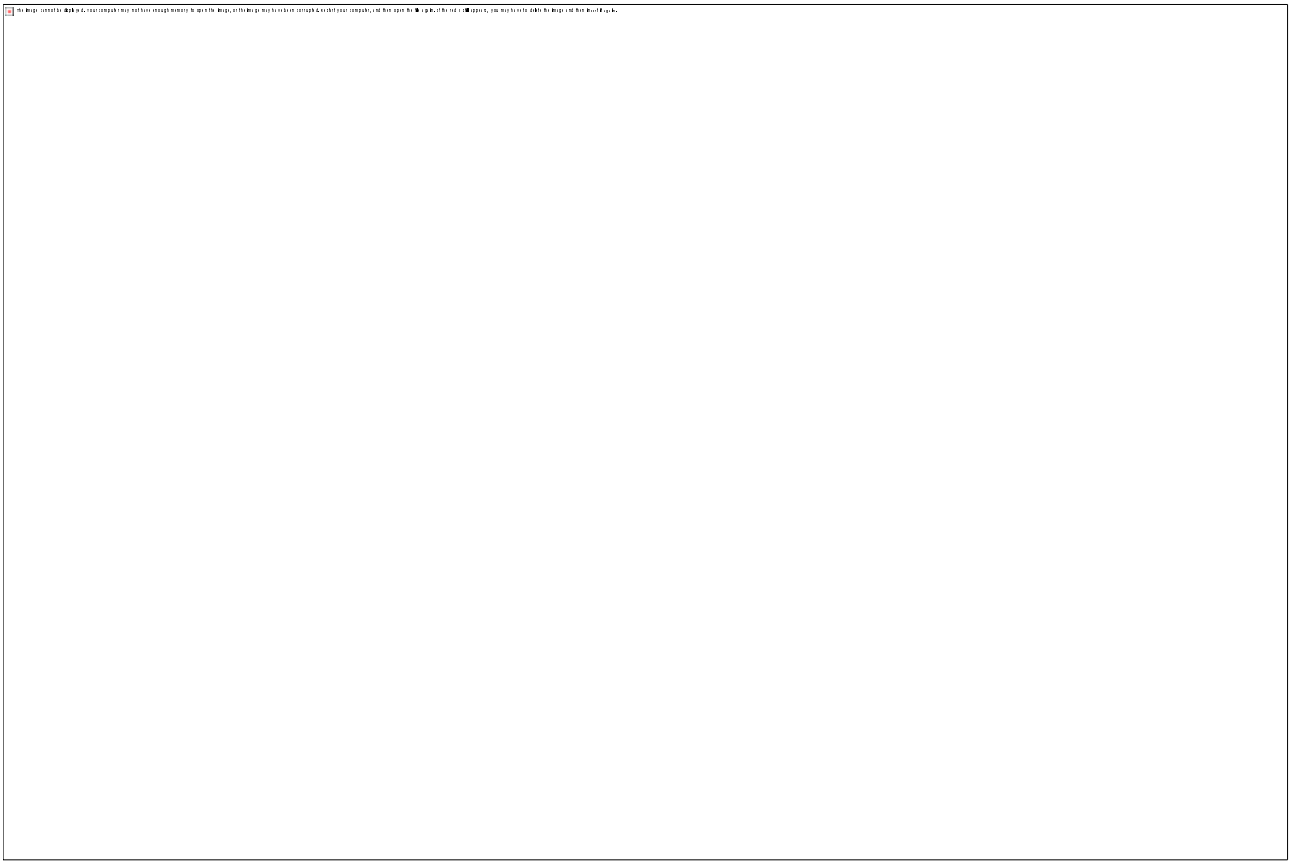

Figure 3. SARS-CoV-2 infection of the brain: no evidence that the virus targets the brain vasculature. Brainstem, mice infected with SARS-CoV-2 Delta at 10^2 PFU (cohort 2.1) or 10^3 PFU (cohort 2.2), 6, 7, or 8 dpi. **A, B)** Transmission electron microscopy. **A)** Animal 2.1.3. Unaltered capillary (small arrows: endothelial layer, arrowheads: basement membrane; E: erythrocyte) with adjacent virus infected cell (morphology consistent with neuron) containing viral particles (arrows), replication-associated membranous structures (asterisk: double-membrane vesicles), and an electron dense aggregate consistent with cytoplasmic accumulation of nucleocapsid protein (NP) (Carossino et al. 2022). **B)** Animal 2.2.5. Unaltered (post-capillary) venule with adjacent virus infected neuron (asterisk: nucleus) with membrane-bound viral particles (arrowheads). Inset: higher magnification of viral particles in (distended) organelles (arrowhead). **C, D)** Immune-EM. Animal 2.1.5. Unaltered post-capillary venule adjacent to virus infected cells (morphology consistent with neuron). **C)** A monocyte/macrophage (C: asterisk) is present in the perivascular space (arrow with two tips). The infected neuron contains labelled membrane-bound viral particles (arrowheads) and strongly labelled cytoplasmic aggregates (consistent with accumulation of nucleocapsid protein (N)). **D)** Adjacent to the vessels (arrowheads: basement membrane) are astrocytic endfeet (asterisks) without evidence of viral particles or nucleocapsid protein deposition. An adjacent cell (morphology consistent with neuron) contains viral particles (arrows).

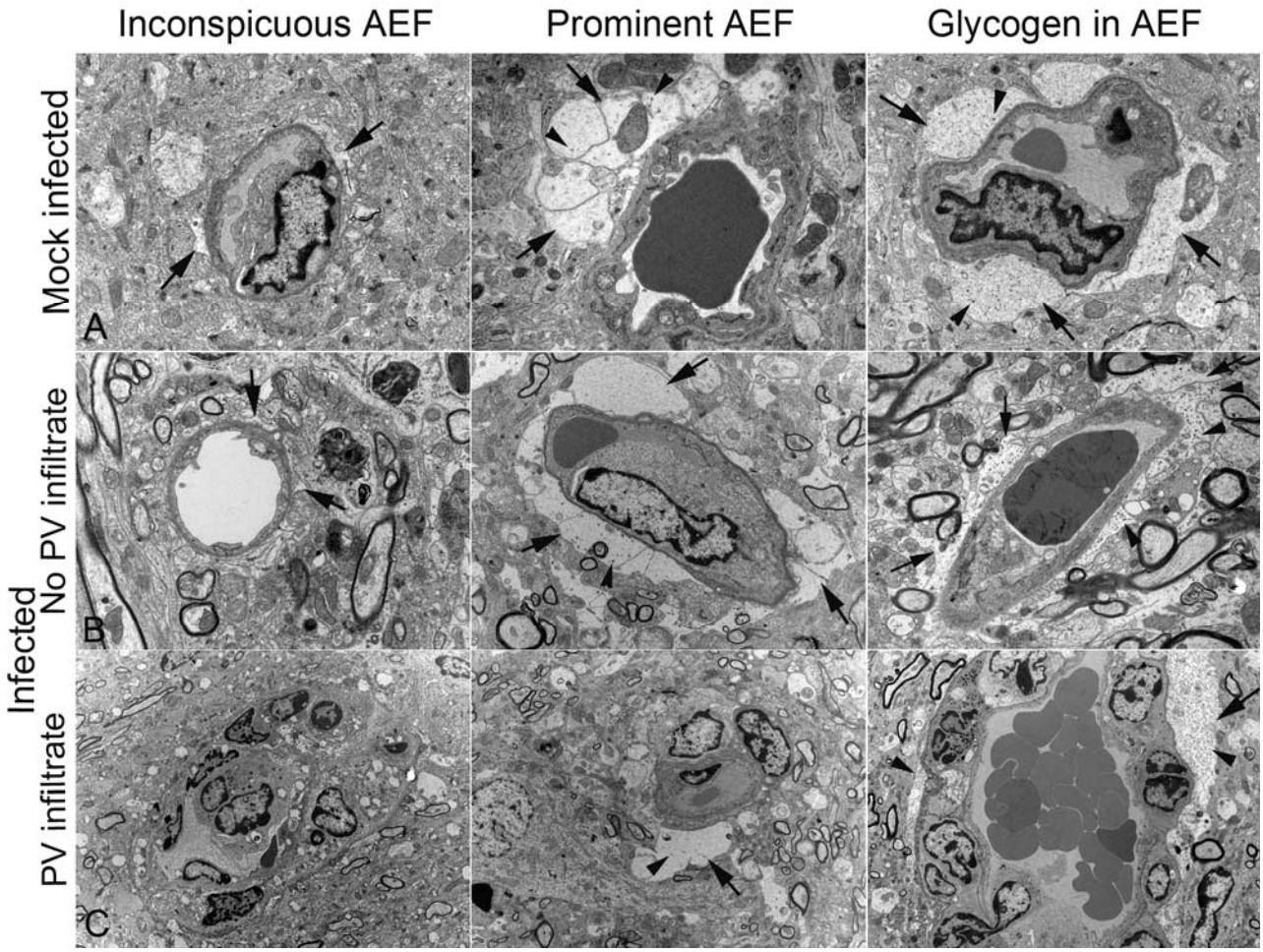

Figure 4. Morphological appearance of the astrocytic endfeet (AEF) of small calibre vessels. Brainstem. **A)** Mock infected mice (animals 2.3.1 and 2.3.2). AEF (arrows) are either inconspicuous or prominent. Some of the latter contain finely granular electron-dense material compatible with glycogen granules (arrowheads). **B, C)** Mice infected with SARS-CoV-2 Delta at 10^2 PFU (cohort 2.1; animals 2.1.1, 2.1.4, 2.1.8) or 10^3 PFU (cohort 2.2; animal 2.2.5), 6, 7, or 8 dpi. Regardless of the absence (B) or presence (C) of perivascular (PV) infiltrates, AEF (arrows) are either inconspicuous or prominent. They contain finely granular electron-dense material compatible with glycogen granules (B, C: right column; arrowheads) the amount of which appears higher than in the control brain. Transmission electron microscopy.

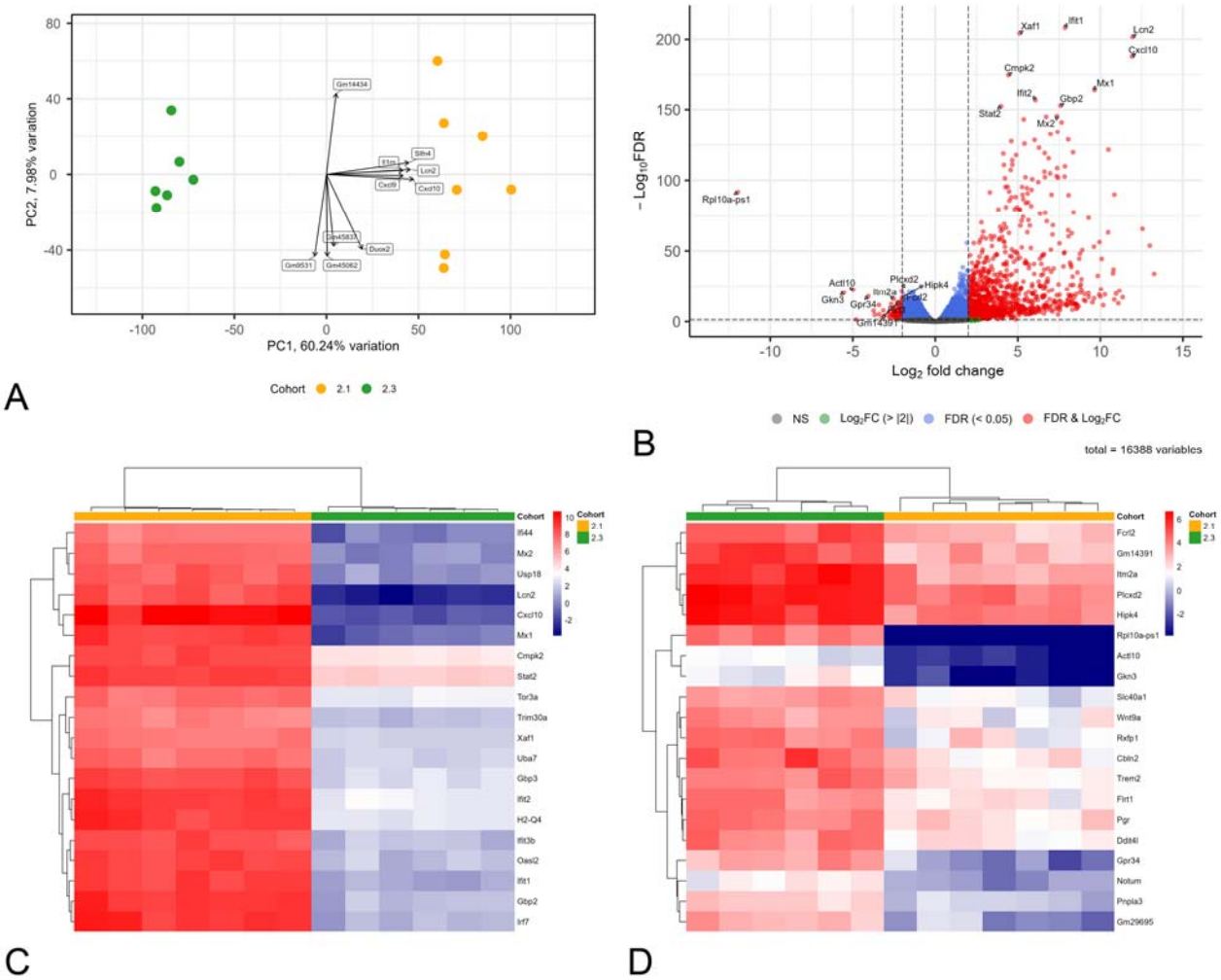

Figure 5. Results of the bulk RNA sequencing analysis in SARS-CoV-2 Delta infected brains. Mice infected with SARS-CoV-2 Delta at 10^2 PFU (cohort 2.1) and mock infected mice (cohort 2.3). **A)** The PCA biplot shows the clustering of the samples in their relative cohort, as well as the loadings. **B)** Volcano plot showing the distribution of the investigated genes, regarding the FDR (0.05) and the log_2FC (|2|). **C, D)** Heatmaps showing the 20 most significantly up- (C) and downregulated (D) genes.

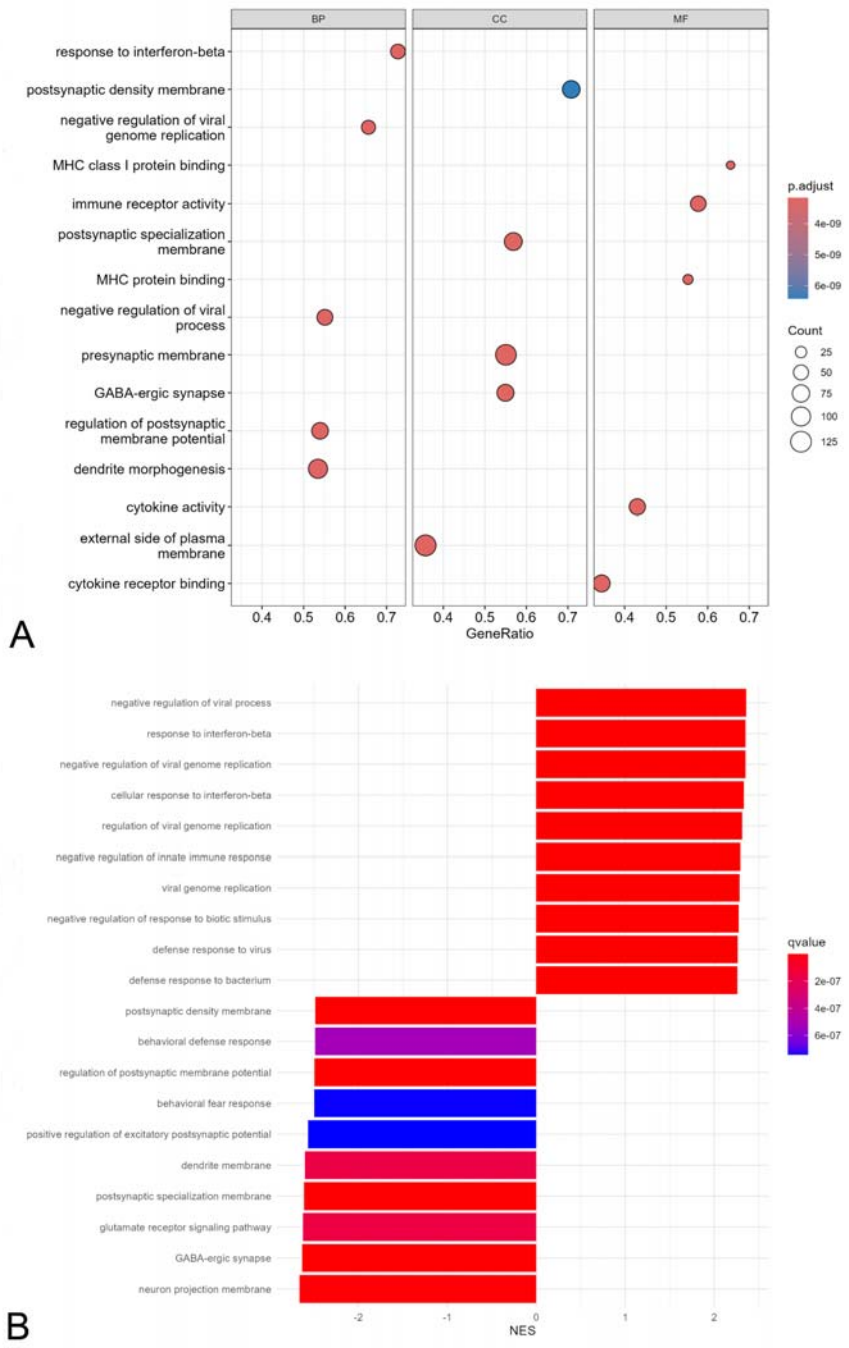

Figure 6. GO GSEA pathway enrichment analysis in SARS-CoV-2 Delta infected brains. Mice infected with SARS-CoV-2 Delta at 10^2 PFU (cohort 2.1) and mock infected mice (cohort 2.3). **A)** Illustration of the top 5 enriched pathways for each ontology (BP, CC, MF). **B)** Illustration of the top and bottom 10 enriched pathways sorted on the NES. BP: biological process; CC: cellular component; MF: molecular unction; NES: normalised enrichment score.

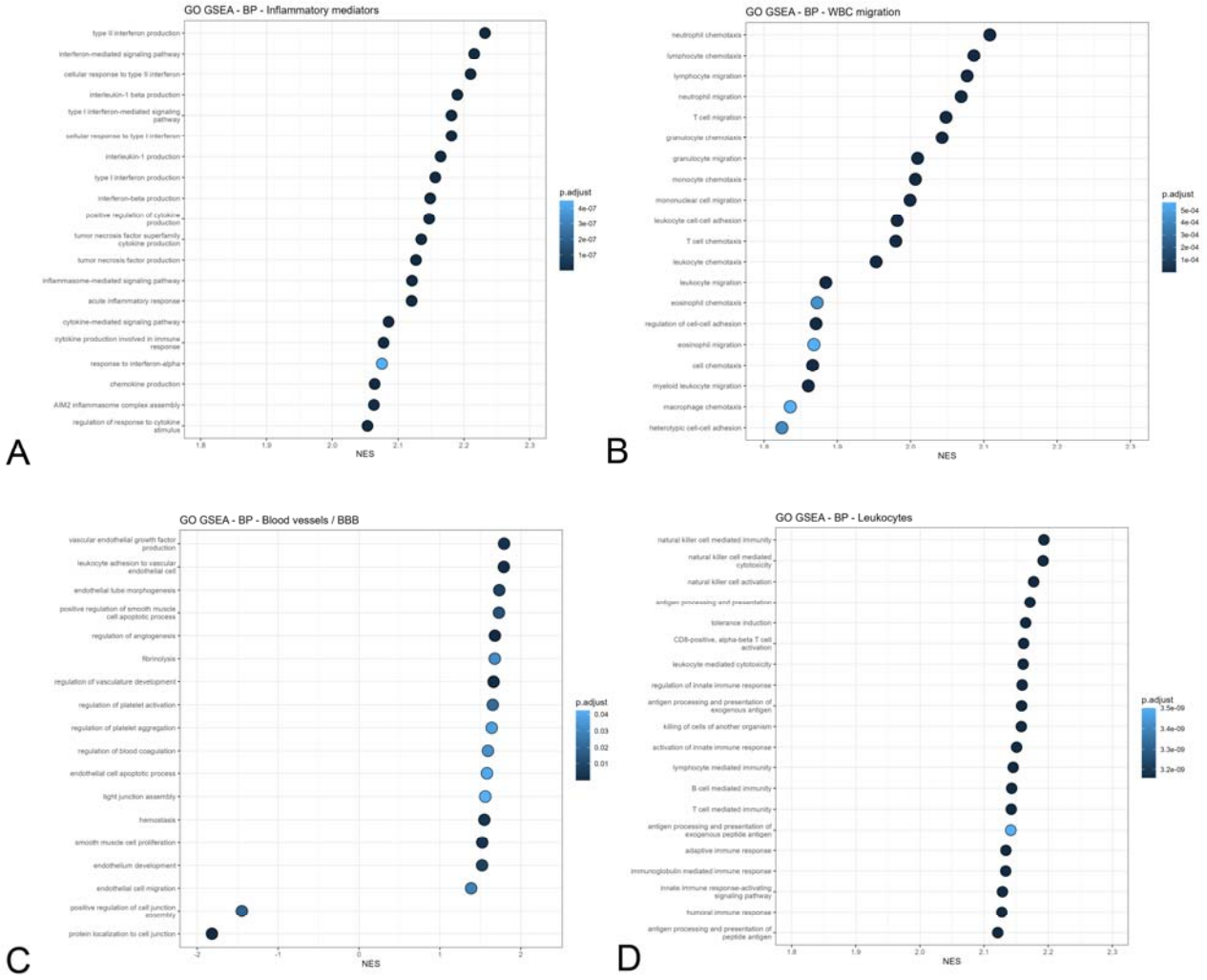

Figure 7. GO GSEA pathway enrichment analysis in SARS-CoV-2 Delta infected brains based on selected keywords. Mice infected with SARS-CoV-2 Delta at 10^2 PFU (cohort 2.1) and mock infected mice (cohort 2.3). Illustration of the top 20 (or 18) enrich ed pathways for the BP ontology and sorted on the NES. **A)** Inflammatory mediators. **B)** Leukocyte migration. **C)** Leukocytes. **D)** Blood vessels – blood-brain barrier. BP: biological process; NES: normalised enrichment score.